Petroleum Science 23 (2026) 2501–2526

Contents lists available at ScienceDirect

Petroleum Science

journal homepage: www.keaipublishing.com/en/journals/petroleum-science

Original Paper

Semi-supervised learning for AVO inversion with bidirectional spatial feature constraints

Ying-Tian Liu [a,b], Yong Li [a,b,*], Jun-Heng Peng [a,b], Jian-Yong Xie [a,b], Xian-Qiong Chen [a,b]

[a] Key Lab of Earth Exploration & Information Techniques of Ministry of Education, Geophysical Institute, Chengdu University of Technology, Chengdu, 610059, Sichuan, China
[b] State Key Laboratory of Oil and Gas Reservoir Geology and Exploitation, Chengdu University of Technology, Chengdu, 610059, Sichuan, China

ARTICLE INFO

Article history:
Received 31 July 2025
Received in revised form
17 November 2025
Accepted 6 January 2026
Available online 9 January 2026

Edited by Meng-Jiao Zhou

Keywords:
AVO inversion
Deep learning
Spatial feature constraints
Semi-supervised learning

ABSTRACT

Prestack amplitude variation with offset (AVO) inversion using one-dimensional convolutional neural networks often lacks lateral continuity. While two-dimensional methods improve this, they are limited to unidirectional spatial correlations from well to non-well locations. To overcome these limitations, we propose a semi-supervised learning approach with bidirectional spatial feature constraints (BSFC-SSL). Our method introduces a label-annihilation operator and a dedicated spatial feature network to establish bidirectional information flow between well and non-well locations, thereby capturing more complex spatial patterns in seismic data. Integrated with semi-supervised learning and low-frequency constraints, the BSFC-SSL framework enhances both stability and generalization. Experiments on synthetic and field data demonstrate that our method achieves superior lateral continuity and inversion accuracy compared to conventional one- and two-dimensional deep learning techniques.

1. Introduction

Amplitude variation with offset (AVO) analysis has long been a crucial tool in hydrocarbon exploration and reservoir characterization, providing valuable insights into the elastic properties of subsurface formations (Alemie and Sacchi, 2011; Meng et al., 2021). Zoeppritz (1919) conducted the first theoretical investigation into AVO technology. By examining the variation in reflection coefficients with incidence angles, he analyzed the parameter changes in the media on either side of the reflection interface and formulated the Zoeppritz equations. Although these equations provide precise calculations of reflection coefficients, their complex expressions make them challenging to apply directly to AVO inversion of real-world data. Consequently, researchers have developed simplified versions of the Zoeppritz equations from various perspectives (Bortfeld, 1961; Smith and Gidlow, 1987; Gray and Andersen, 2000). Model-driven AVO inversion is a method to extract seismic parameters such as P-wave velocity, S-wave velocity, and density from prestack seismic data based on AVO theory. The traditional modeldriven AVO inversion method used a linear method to establish the mapping between the reflection coefficient and parameters. Ikelle (1995) proposed a linear AVO inversion algorithm based on the least-squares method for processing 3D multi-migration seismic data. Downton and Ursenbach (2006) proposed a linearized AVO inversion method that can accurately deal with the reflection coefficients of the above critical angles, considering the amplitude and phase changes with the migration. However, AVO inversion is an ill-posed problem with many difficulties, such as limited data bandwidth, noise corruption, and incomplete data coverage (Yin et al., 2016; She et al., 2019). To overcome this problem, many methods have been proposed, including Bayesian probabilistic inversion (Zong et al., 2016; Li et al., 2022a), exhaustive searching (Jensen et al., 2016; Misra and Sacchi, 2008). Gradient-based algorithms, such as the limited-memory BFGS (L-BFGS) method, are commonly employed for nonlinear inverse problems (Ahmed et al., 2022, 2023). These techniques typically involve the construction of a geological or petrophysical model, which is then used to derive synthetic seismic responses that are matched to the observed data through an iterative optimization process (Avseth et al., 2016; Feng et al., 2025). While these inversion methods have demonstrated promising results, they are computationally intensive, and their

* Corresponding author.
E-mail address: liyong07@cdut.edu.cn (Y. Li).
Peer review under the responsibility of China University of Petroleum (Beijing).

https://doi.org/10.1016/j.petsci.2026.01.005

outcomes are highly sensitive to the selection of the initial model (Li et al., 2022b; Zhang et al., 2022).

Deep learning (DL), known for its ability to represent complex features and perform nonlinear mapping, has become a key research focus in seismic exploration (Yang and Ma, 2019; Wang et al., 2020a). In this field, DL techniques have achieved promising results in various aspects, including reservoir parameter prediction (Chen et al., 2020; Masroor et al., 2023), fault identification (Xiong et al., 2018; Wang et al., 2024), noise attenuation (Liao et al., 2023; Zhao et al., 2018), and stratigraphic interpretation (Di et al., 2020; Gu et al., 2023). In recent years, DL has also been developed in seismic inversion. Das et al. (2019) employed a one-dimensional convolutional neural network (CNN) for seismic inversion. Mustafa et al. (2019) proposed a workflow for impedance prediction utilizing temporal convolutional networks (TCN). Cao et al. (2018) proposed a DL-based AVO inversion method with Dropout regularization, enhancing the prediction accuracy and stability of P-wave velocity, S-wave velocity, and density. As shown in Fig. 1(a), the earliest DL inversion method was to extract the characteristics of prediction parameters from single-trace seismic data and utilize well-log data to constrain these characteristics, thereby establishing a non-linear mapping between seismic data and elastic parameters (Zheng et al., 2019; Zhang et al., 2021).

In practical applications, the availability of labeled data is limited due to the high cost of well-log data. To solve the challenge of limited labeled data, scholars have introduced various constraints. Alfarraj and AlRegib (2019) proposed a semi-supervised gate recurrent unit (GRU) framework based on seismic forward modeling. Notably, semi-supervised learning (SSL) has achieved remarkable success in related geophysical tasks, such as complex lithofacies identification (Dong et al., 2024) and fracture detection in tight sandstones (Dong et al., 2020), where limited well-log data similarly restricts model performance. Liu et al. (2025a) further integrated the semi-supervised TCN with Nash game theory (Navon et al., 2022) to effectively mitigate gradient conflicts in AVO inversion. In addition, physics-guided neural networks have been successfully applied to both prestack and poststack inversion (Sun et al., 2021; Ge et al., 2024). Many semi-supervised inversion methods incorporating model-based forward modeling have been proposed to address a variety of geological inverse problems (Guo et al., 2019; Fabien-Ouellet and Sarkar, 2020). These methods integrate seismic data constraints through physics-based forward modeling; however, they often rely on the accurate estimation of the seismic wavelet, which remains a significant challenge in practical applications. To overcome this limitation, Yuan et al. (2022) proposed employing a network as an alternative to the traditional physical forward modeling. Shi et al. (2024) proposed a

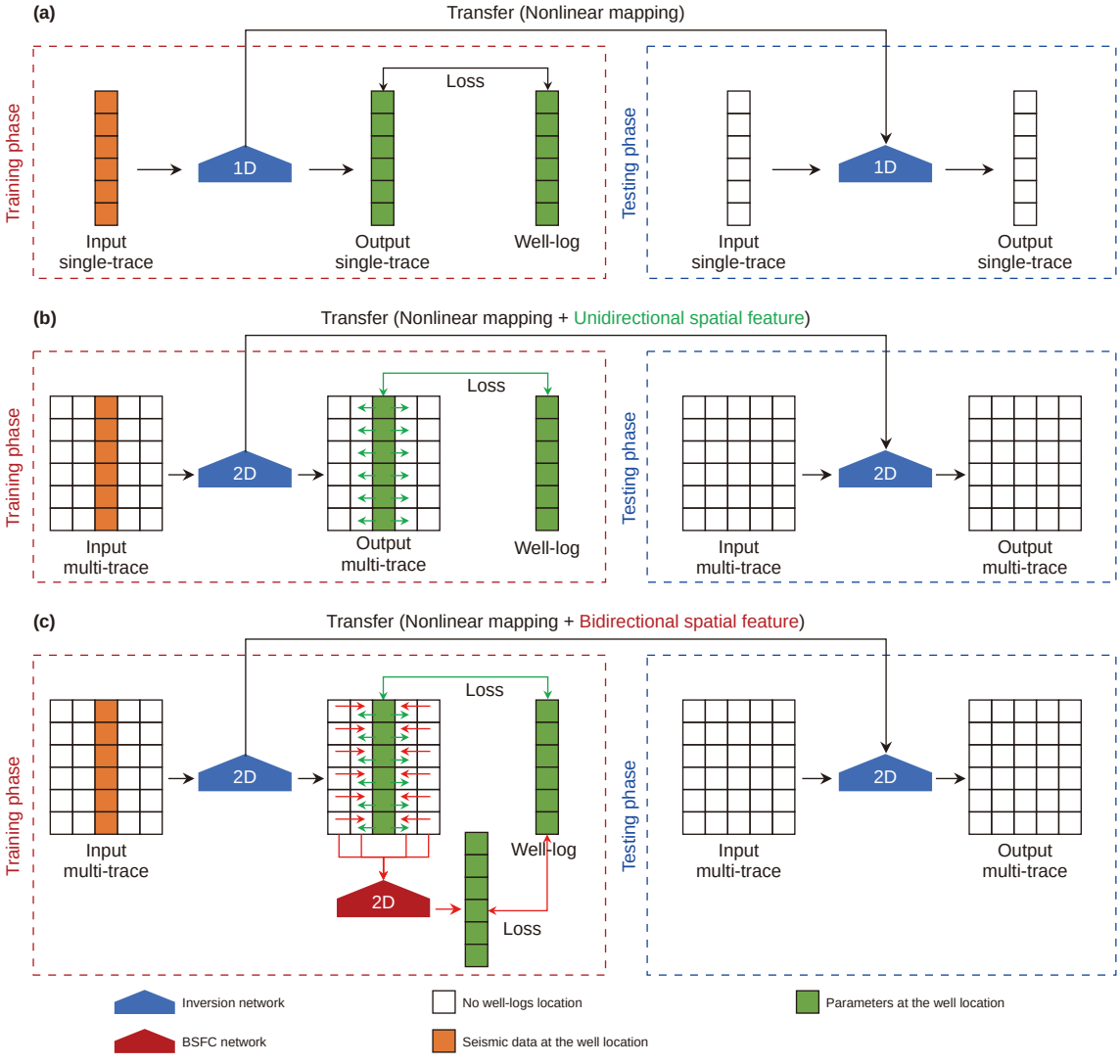

Fig. 1. Training and testing workflows of different inversion methods. **(a)** 1D data-driven inversion, **(b)** 2D data-driven inversion, and **(c)** the proposed method.

semi-supervised closed-loop seismic inversion (CL-SSL) that uses a forward network to constrain the inversion network, effectively utilizing both labeled and unlabeled data. Wang et al. (2023) proposed an AVO inversion method based on the closed-loop seismic inversion framework, capable of accurately inverting the P-wave velocity, S-wave velocity, and density. Liu et al. (2025b) integrated a closed-loop framework with frequency-phase-domain information to resolve thin layers and weak reflection areas. Although these methods map single-trace seismic data to corresponding parameters, they ignore spatial correlations between traces, leading to vertical artifacts in inversion results. As shown in Fig. 2(a), 1D data-driven inversion produces discontinuous spatial features, failing to capture the smooth lateral transitions of geological structures. To improve lateral continuity, high-dimensional convolutional kernels were introduced to establish correlations between multi-trace seismic data and multi-trace parameters. Wu et al. (2021) proposed an improved DL method based on two-dimensional CNN that significantly improves the stability of impedance prediction. Wang et al. (2022b) introduced a two-dimensional semi-supervised inversion method that improves the accuracy and spatial continuity of seismic inversion. Mustafa et al. (2021) proposed a joint learning strategy that integrates a two-dimensional TCN and spatial contexts (SC-JL), significantly enhancing the robustness and spatial consistency of the estimated parameters. Liu et al. (2024) proposed a two-dimensional Transformer framework with transfer pretraining to improve the stability of prestack AVO inversion. Li et al. (2024) developed a three-dimensional residual structure, which is used for efficient 3D seismic impedance inversion.

These methods process multi-trace seismic data using high-dimensional convolutional kernels and produce multi-trace prediction parameters. As shown in Fig. 1(b), during the training process, multi-trace seismic data is used as the input, and multi-trace predicted parameters are output. The predicted parameters at well locations are constrained by the available well-log data, while those at non-well locations are inferred from the sparse representation of well-log information and the spatial reasoning capability of the two-dimensional network (Dou et al., 2021, 2022). As illustrated in Fig. 2(b), although these 2D inversion methods improve the lateral continuity of inversion results, they mainly rely on what we term “unidirectional spatial features”. This refers to a one-way inference process where spatial correlations can only be learned and transferred from the well-log locations (with known labels) to the non-well locations (without labels). In geologically complex areas, this unidirectional flow of information is often insufficient as it fails to capture the mutual spatial dependencies inherent in the subsurface.

To overcome this limitation and fully exploit the spatial features in seismic data, we propose a semi-supervised learning framework with bidirectional spatial feature constraints (BSFC-SSL). The core of our approach is the establishment of “bidirectional spatial features”, which enable two-way information flow between well and non-well locations. As illustrated in Fig. 1(c), the BSFC-SSL architecture integrates an inversion network, a forward network, and a bidirectional spatial feature constraint (BSFC) network. The inversion network first maps multi-trace inputs to multi-trace outputs. Subsequently, the BSFC network explicitly enforces bidirectional spatial relationships by utilizing the predicted parameters at non-well locations to infer and refine the parameters at well locations (see Fig. 2(c)), in addition to the conventional well-to-non-well inference. This dedicated convolutional operation ensures that spatial features are transferred in both directions, resulting in a more complete and geologically consistent spatial model. Additionally, to address the limited availability of labeled data in real-world applications, we incorporate a semi-supervised structure that leverages seismic data at non-well locations to improve generalization. Moreover, a low-frequency model constraint is employed to stabilize the recovery of low-frequency components and improve inversion accuracy.

The article is organized as follows. First, we present the theoretical foundation of the BSFC-SSL method, including the overall framework, the semi-supervised inversion structure, the bidirectional spatial feature constraints, the adaptive multi-loss reweighting strategy, and the detailed workflow and network architecture. Then, we compare the AVO inversion results of the model-based method, the one-dimensional deep learning method, the two-dimensional deep learning method, and the proposed method. Next, the field data application is provided to demonstrate the feasibility of our method for field data. Finally, we draw the key conclusions.

2. Theory

2.1. Prestack AVO inversion and forward

AVO is a crucial technique for characterizing subsurface reservoirs by analyzing the variation in seismic wave amplitudes with offset. Its theoretical foundation is the convolution model, which can be expressed as

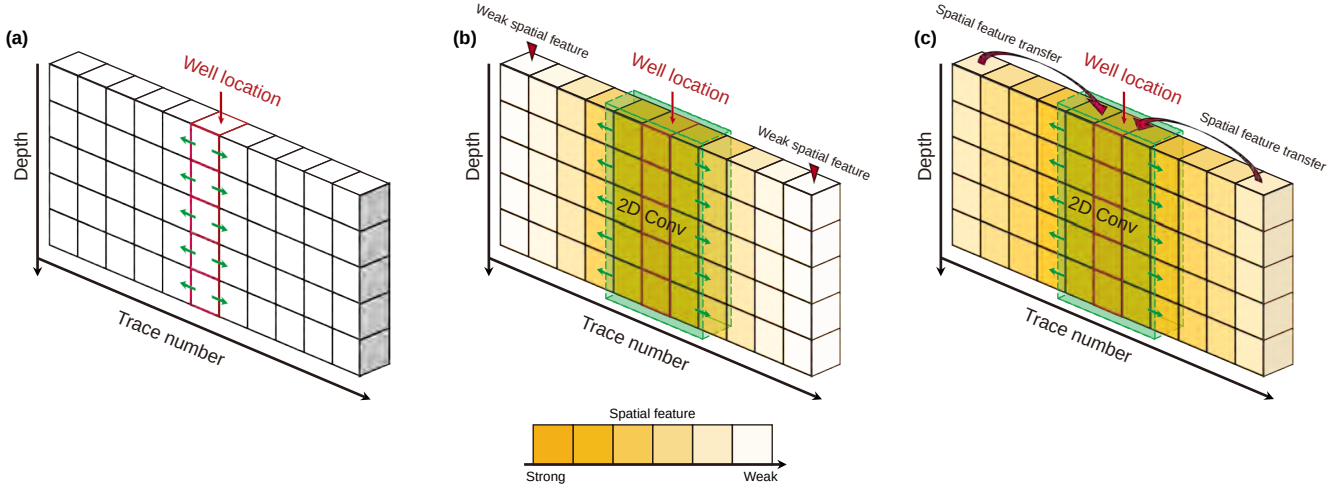

Fig. 2. Spatial feature differences among various methods. **(a)** 1D data-driven inversion, **(b)** 2D data-driven inversion, and **(c)** the proposed method.

$$\mathbf{D} = \mathbf{W}*\mathbf{R}_{PP} \tag{1}$$

where * represents convolution of matrices, **D** represents seismic data, **W** is the seismic wavelet, and $\mathbf{R}_{PP}$ denotes the P-wave reflection coefficient. According to the Zoeppritz equations, $\mathbf{R}_{PP}$ can be explicitly calculated from the P-wave velocity, S-wave velocity, and density. Therefore, the reflection coefficient can be simplified as

$$\mathbf{R}_{PP} = \mathbf{fm} \tag{2}$$

where **m** is a vector set of elastic parameters: P-wave velocity, S-wave velocity, and density, represented as $\mathbf{m} = [V_P, V_S, \rho]^T$, **f** represents the mapping matrix between seismic parameters and reflection coefficients. By substituting Eq. (2) into Eq. (1), the general form of the forward equation in AVO theory can be expressed as

$$\mathbf{D} = \mathbf{W}*\mathbf{fm} = \mathbf{Gm} \tag{3}$$

where **G** represents the forward operator.

When the mapping matrix **G** is invertible and the influence of the seismic wavelet is disregarded, the inversion result can be expressed as

$$\mathbf{m} = \mathbf{G}^{-1}\mathbf{D} \tag{4}$$

where $\mathbf{G}^{-1}$ represents the inverse operator of **G**. However, in practical AVO inversion scenarios, the mapping operator $\mathbf{G}^{-1}$ is typically non-invertible due to the ill-posed nature of the problem.

2.2. Overall framework of the BSFC-SSL

The proposed BSFC-SSL framework is designed to overcome the key limitations of existing deep learning-based AVO inversion methods. Our approach integrates three core innovations into a cohesive system to achieve high-fidelity inversion results with superior lateral continuity, especially under limited well-log constraints. The overall architecture is illustrated in Fig. 3, and its core concepts are organized as follows: I. Semi-supervised inversion structure: To tackle the scarcity of labeled well-log data, we adopt a semi-supervised learning paradigm centered on a closed-loop structure. This structure comprises an inversion network that maps seismic data to elastic parameters and a forward network that reconstructs seismic data from these parameters. By cycling both labeled and unlabeled data through this loop, the model enforces physical consistency, effectively leveraging abundant unlabeled seismic traces to improve generalization and stability beyond the sparse well locations. II. Bidirectional spatial feature constraints: Moving beyond conventional 2D methods that rely on unidirectional inference (from wells to non-wells), we introduce a dedicated Bidirectional spatial feature constraints (BSFC) network. This component enables mutual information flow between well and non-well locations. The core mechanism involves a label annihilation operator, which masks the predicted parameters at the well location, forcing the BSFC network to recover them from the surrounding traces. This process explicitly establishes and leverages bidirectional spatial correlations, capturing more geologically consistent subsurface patterns. III. Adaptive multi-loss reweighting via the GradNorm strategy: The training of the overall framework involves optimizing a composite objective function that combines the supervised inversion loss, the seismic reconstruction loss, and the bidirectional spatial constraint loss. These losses operate on different scales and can imbalance the training process. To ensure all tasks learn concurrently and effectively, we employ a gradient normalization (GradNorm) strategy, which dynamically adjusts the weight of each loss term based on its training progress, leading to more stable and efficient convergence. By integrating these three components, the BSFC-SSL framework achieves a significant improvement in inversion accuracy and spatial continuity, as will be demonstrated in the subsequent experiments. The following subsections will delve into the details of each component.

2.3. Semi-supervised seismic inversion structure

When deep learning is applied to AVO inversion, the objective is to learn a data-driven approximation of the inverse mapping. Instead of directly computing the mathematical inverse $\mathbf{G}^{-1}$, we employ a neural network to represent this approximation. This is mathematically expressed as

$$\mathbf{m} = \mathscr{I}_w(\mathbf{D}) \tag{5}$$

where $\mathscr{I}_w$ denotes the inversion network, and w denotes the trainable network parameters. The network can perform supervised learning using well-log data, with the objective function expressed as

$$J(\mathscr{I}_w) = \min_{\mathscr{I}_w} ||\mathbf{m}_l - \mathscr{I}_w(\mathbf{D}_l)||_2^2 \tag{6}$$

where $||\cdot||_2^2$ denotes the L_2 norm, $\mathbf{m}_l$ represents the elastic parameters from well-log and $\mathbf{D}_l$ denotes the labeled seismic data at the well location.

However, the proportion of well-log data is extremely small compared to the entire seismic dataset. This leads to a significant shortage of training data, which significantly affects inversion accuracy and limits the practical application of purely supervised learning methods. To overcome the inherent limitations of supervised learning under such extreme label scarcity, we introduce a semi-supervised strategy centered on a learned forward network. This strategy leverages the abundant unlabeled seismic data by constructing a self-consistent cycle: the inversion network generates pseudo-labels from unlabeled data, which are then fed into the forward network to reconstruct the original seismic input. This physical consistency constraint acts as a powerful regularizer. In line with recent advances that mitigate the deficiencies of conventional model-based forward modeling (Downton et al., 2019; Liu et al., 2023; Feng et al., 2025), we construct a data-driven forward network, expressed as

$$\mathbf{D} = \mathscr{F}_w(\mathbf{m}) \tag{7}$$

where $\mathscr{F}_w$ represents the forward network. Similarly, the forward network can utilize well-log data for supervised learning. Meanwhile, it can be combined with the inversion network for unsupervised learning. The objective function is defined as

$$J(\mathscr{F}_w, \mathscr{I}_w) = \min_{\mathscr{F}_w, \mathscr{I}_w} \left\{ \begin{array}{l} |\mathbf{D}_l - \mathscr{F}_w(\mathbf{m}_l)||_2^2 + \\ |\mathbf{D}_u - \mathscr{F}_w(\mathscr{I}_w(\mathbf{D}_u))||_2^2 \end{array} \right\} \tag{8}$$

where $\mathbf{D}_u$ represents the unlabeled seismic data, which refers to the seismic data obtained at locations other than the well site. The first and second terms in Eq. (8) are used to compute the seismic data matching losses for seismic traces adjacent to the wells and those not adjacent to the wells, respectively.

Additionally, low-frequency information captures the macroscopic features of the subsurface geological structure, thereby providing critical constraints for the inversion process and reducing the non-uniqueness of the inversion results (Fu et al.,

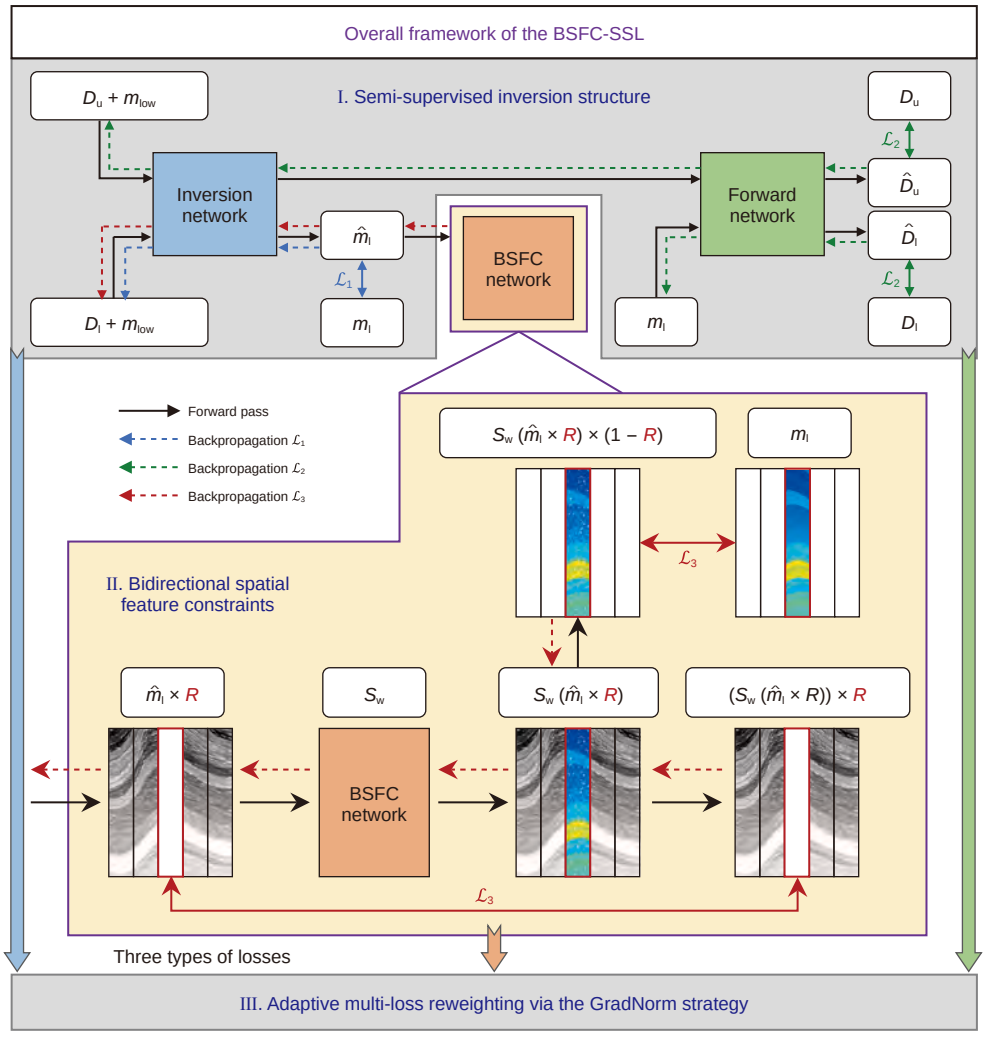

Fig. 3. Overall framework of the BSFC-SSL.

2024). By integrating a low-frequency model into the inversion network and combining it with seismic data as input, and by merging Eqs. (6) and (8), the complete semi-supervised objective function can be formulated as follows:

$$J(\mathscr{I}_w, \mathscr{F}_w) = \min_{\mathscr{I}_w} \left|\left|\mathbf{m}_\mathrm{l} - \mathscr{I}_w(\mathbf{D}_\mathrm{l} \oplus \mathbf{m}_\mathrm{low})\right|\right|_2^2 + \min_{\mathscr{F}_w, \mathscr{I}_w} \left\{ \begin{array}{l} \left|\left|\mathbf{D}_\mathrm{l} - \mathscr{F}_w(\mathbf{m}_\mathrm{l})\right|\right|_2^2 + \\ \left|\left|\mathbf{D}_\mathrm{u} - \mathscr{F}_w(\mathscr{I}_w(\mathbf{D}_\mathrm{u} \oplus \mathbf{m}_\mathrm{low}))\right|\right|_2^2 \end{array} \right\} \tag{9}$$

where $\mathbf{m}_\mathrm{low}$ is the low-frequency model and $\oplus$ represents the channel-wise concatenation of the seismic data $\mathbf{D}$ and the low-frequency model $\mathbf{m}_\mathrm{low}$, which serves as the multi-channel input to the network.

2.4. Bidirectional spatial feature constraints

To establish the mapping of bidirectional spatial features between the predicted parameters at well locations and those at non-well locations, we propose a bidirectional spatial feature constraint method. The matrix forms of ml and $\mathscr{I}_w(\mathbf{D}_\mathrm{l} \oplus \mathbf{m}_\mathrm{low})$ in Eq. (9) are given by

$$\mathbf{m}_\mathrm{l} = \begin{bmatrix} & & & & & & \\ 0 & \cdots & 0 & m_{\frac{M+1}{2},1} & 0 & \cdots & 0 \\ \vdots & \ddots & \vdots & \vdots & \vdots & \ddots & \vdots \\ 0 & \cdots & 0 & m_{\frac{M+1}{2},N} & 0 & \cdots & 0 \\ & & & & & & \end{bmatrix}_{N\times M}$$

$$\widehat{\mathbf{m}} = \mathscr{I}_w(\mathbf{D}_\mathrm{l} \oplus \mathbf{m}_\mathrm{low}) = \begin{bmatrix} \widehat{m}_{1,1} & \cdots & \widehat{m}_{\frac{M+1}{2},1} & \cdots & \widehat{m}_{M,1} \\ \vdots & \ddots & \vdots & \ddots & \vdots \\ \widehat{m}_{1,N} & \cdots & \widehat{m}_{\frac{M+1}{2},N} & \cdots & \widehat{m}_{M,N} \end{bmatrix}_{N\times M} \tag{10}$$

where $\widehat{\mathbf{m}}$ denotes the predicted parameter, N and M represent the depth and width of $\mathbf{m}_\mathrm{l}$, respectively. According to Eq. (10), the well-log label only constrains the first trace at the position of $\frac{M+1}{2}$, corresponding to the center trace. In the discussion section, we

also test well-log positions other than the center trace. Predicted parameters far from the well-log position rely on the sparsity of the data, often resulting in weak spatial features. To address this, we introduce a label annihilation operator **R**, strategically designed to enhance spatial feature learning. Mathematically, **R** is defined as an $N \times M$ matrix:

$$\mathbf{R} = \begin{bmatrix} 1 & \cdots & 1 & 0 & 1 & \cdots & 1 \\ \vdots & \ddots & \vdots & \vdots & \vdots & \ddots & \vdots \\ 1 & \cdots & 1 & 0 & 1 & \cdots & 1 \end{bmatrix}_{N\times M} \tag{11}$$

The matrix **R** is designed to set the values of the central trace (corresponding to the logging position) to zero, while keeping the adjacent traces unchanged. By applying element-wise multiplication $\widehat{\mathbf{m}} \times \mathbf{R}$, we mask the predicted parameters of the middle trace (as illustrated in "II. Bidirectional spatial feature constraints" in Fig. 3), effectively removing well-log constraints from this trace. This forces the network to leverage spatial correlations from surrounding traces, enabling bidirectional feature transfer between well and non-well locations.

To recover the masked middle-trace data using adjacent traces, we construct a bidirectional spatial feature constraint network $\mathscr{S}_w$. To ensure stable network convergence, we introduce a self-consistency (Pourpanah et al., 2022; Wang et al., 2022c; Peng et al., 2024), which enforces consistency between the input and output of the BSFC network. The objective function is defined as

$$J(\mathscr{S}_w) = \min_{\mathscr{S}_w} \left\{ \begin{array}{l} ||\mathbf{m}_l - (\mathscr{S}_w(\widehat{\mathbf{m}}_l \times \mathbf{R})) \times (1 - \mathbf{R})||_2^2 \\ +||\widehat{\mathbf{m}}_l \times \mathbf{R} - (\mathscr{S}_w(\widehat{\mathbf{m}}_l \times \mathbf{R})) \times \mathbf{R}||_2^2 \end{array} \right\} \tag{12}$$

where $\times$ denotes element-wise matrix multiplication. The operation $\widehat{\mathbf{m}}_l \times \mathbf{R}$ applies a masking operator to the middle seismic trace constrained by the well-log (as illustrated in "II. Bidirectional spatial feature constraints" in Fig. 3), setting its values to zero. This masked data is subsequently fed into the BSFC network, denoted as $\mathscr{S}_w$, which processes the input to produce $\mathscr{S}_w(\widehat{\mathbf{m}}_l \times \mathbf{R})$. As shown in the upper part of the figure, the error between $\mathscr{S}_w(\widehat{\mathbf{m}}_l \times \mathbf{R}) \times (1 - \mathbf{R})$ and the well-log label $\mathbf{m}_l$ is calculated. This step aims to ensure that the network can recover the information in the masked area, thus achieving a better match with the well-log label. Meanwhile, the error between $\mathscr{S}_w(\widehat{\mathbf{m}}_l \times \mathbf{R}) \times \mathbf{R}$ and $\widehat{\mathbf{m}}_l \times \mathbf{R}$ is used to ensure the consistency within the non-masked area. These constraints establish the spatial correlation between the predicted parameters through the BSFC network, thereby enabling the bidirectional spatial mapping between the well-log traces and the non-well-log traces.

Furthermore, by combining Eqs. (9) and (12), the total objective function is obtained:

$$J(\mathscr{S}_w, \mathscr{F}_w, \mathscr{S}_w) = \min_{\mathscr{S}_w} \underbrace{||\mathbf{m}_l - \mathscr{S}_w(\mathbf{D}_l \oplus \mathbf{m}_{low})||_2^2}_{\mathscr{L}_1}$$

$$+ \min_{\mathscr{F}_w, \mathscr{S}_w} \underbrace{\left\{ \begin{array}{l} ||\mathbf{D}_l - \mathscr{F}_w(\mathbf{m}_l)||_2^2 + \\ ||\mathbf{D}_u - \mathscr{F}_w(\mathscr{S}_w(\mathbf{D}_u \oplus \mathbf{m}_{low}))||_2^2 \end{array} \right\}}_{\mathscr{L}_2}$$

$$+ \min_{\mathscr{S}_w} \underbrace{\left\{ \begin{array}{l} ||\mathbf{m}_l - (\mathscr{S}_w(\widehat{\mathbf{m}}_l \times \mathbf{R})) \times (1 - \mathbf{R})||_2^2 \\ +||\widehat{\mathbf{m}}_l \times \mathbf{R} - (\mathscr{S}_w(\widehat{\mathbf{m}}_l \times \mathbf{R})) \times \mathbf{R}||_2^2 \end{array} \right\}}_{\mathscr{L}_3} \tag{13}$$

where $\mathscr{L}_1$ denotes the training loss of the inversion network, $\mathscr{L}_2$ denotes the loss from the reconstruction of seismic data, and $\mathscr{L}_3$ denotes the training loss of the BSFC network. The detailed computation of these loss components is summarized in Algorithm 1.

Algorithm 1. Core computation of loss components in BSFC-SSL.

Algorithm 1: Core computation of loss components in BSFC-SSL

1: **Input:** $\{\mathbf{D}_l, \mathbf{m}_l\}$, labeled data; $\{\mathbf{D}_u\}$, unlabeled data; $\{\mathbf{m}_{low}\}$, low-frequency model; I_w, inversion network; F_w, forward network; S_w, BSFC network; **R**, label annihilation operator

2: **Output:** Loss components L_1, L_2, L_3

3: // **Inversion path**

4: $\hat{\mathbf{m}}_l \leftarrow I_w(\mathbf{D}_l \oplus \mathbf{m}_{low})$ // Prediction at well locations

5: $\hat{\mathbf{m}}_u \leftarrow I_w(\mathbf{D}_u \oplus \mathbf{m}_{low})$ // Prediction at non-well locations

6: // **Forward path** (Semi-supervised constraint)

7: $\tilde{\mathbf{D}}_l \leftarrow F_w(\mathbf{m}_l)$

8: $\tilde{\mathbf{D}}_u \leftarrow F_w(\hat{\mathbf{m}}_u)$

9: // **Bidirectional spatial constraint path**

10: $\hat{\mathbf{m}}_l^{masked} \leftarrow \hat{\mathbf{m}}_l \times \mathbf{R}$ // Annihilate center trace

11: $\hat{\mathbf{m}}_l^{rec} \leftarrow S_w(\hat{\mathbf{m}}_l^{masked})$ // Recover via spatial features

12: // **Loss calculation**

13: $L_1 \leftarrow ||\mathbf{m}_l - \hat{\mathbf{m}}_l||_2^2$ // Supervised inversion loss

14: $L_2 \leftarrow ||\mathbf{D}_l - \tilde{\mathbf{D}}_l||_2^2 + ||\mathbf{D}_u - \tilde{\mathbf{D}}_u||_2^2$ // Seismic reconstruction loss

15: $L_3 \leftarrow ||\mathbf{m}_l - (\hat{\mathbf{m}}_l^{rec} \times (1 - \mathbf{R}))||_2^2 + ||\hat{\mathbf{m}}_l^{masked} - (\hat{\mathbf{m}}_l^{rec} \times \mathbf{R})||_2^2$ // BSFC network loss

2.5. Adaptive multi-loss reweighting via the GradNorm strategy

In this study, we employ a composite loss function consisting of three components. Although each term captures a distinct aspect of the seismic inversion task, they typically exhibit different numerical scales and convergence behaviors. Using equal weights for all components may lead to an imbalanced optimization process where certain tasks dominate training. To address this, we adopt the GradNorm strategy (Chen et al., 2018), which adaptively adjusts the weight of each loss term based on the gradient magnitudes with respect to the model parameters. This dynamic reweighting facilitates balanced multi-task learning, promoting both stable and efficient training. The overall loss function is defined as

$$\mathscr{L}_{\text{total}}(t) = \sum_{i=1}^{3} w_i(t)\mathscr{L}_i(t) \tag{14}$$

where $w_i(t)$ denotes the weight assigned to task i at each training step t. To further investigate the influence of network parameters on the loss of each task, we examine the gradient of the weighted single-task loss with respect to the network parameters. Specifically, we define:

$$G_{\text{p}}^{(i)}(t) = \left\| \nabla_{\text{p}} w_i \mathscr{L}_i(t) \right\|_2 \tag{15}$$

where p represents the network parameters, which cover all trainable parameters such as weights and biases in the network. $G_{\text{p}}^{(i)}(t)$ represents the L_2 norm of the gradient of the weighted single-task loss $w_i\mathscr{L}_i(t)$ with respect to the network parameter p. Furthermore, we define a relative inverse training rate of task i as follows:

$$r_i(t) = \frac{\mathscr{L}_i(t)}{\mathscr{L}_i(0)} \Bigg/ \left(\frac{1}{3}\sum_{i=1}^{3} \frac{\mathscr{L}_i(t)}{\mathscr{L}_i(0)} \right) \tag{16}$$

where $r_i(t)$ denotes the relative inverse training rate of task i. It quantifies the relative change in the loss of task i at step t compared to its initial loss, normalized by the average change across all tasks. This $r_i(t)$ is subsequently used in the implementation of GradNorm. GradNorm is implemented through a loss function $\mathscr{L}_{\text{grad}}$, which measures the discrepancy between the actual gradient norm of each task at a given time step and its corresponding target gradient norm. This loss is computed across all tasks and summed to yield the final GradNorm loss, defined as

$$\mathscr{L}_{\text{grad}}(t; w_i(t)) = \sum_{i=1}^{3} \left(G_{\text{p}}^{(i)}(t) - \overline{G}_{\text{p}}(t) \times [r_i(t)]^{\alpha} \right) \tag{17}$$

where $\overline{G}_{\text{p}}(t)$ denotes the average gradient norm across tasks, represented as $\overline{G}_{\text{p}}^{(i)}(t) = \frac{1}{3}\sum_{i=1}^{3} G_{\text{p}}^{(i)}(t)$. The term $r_i(t)$ is a balancing factor that adjusts the gradient magnitude for task i; a larger value of $r_i(t)$ indicates a need to increase the gradient for task i, thereby accelerating its training. The hyperparameter α is used to adjust the training speed of tasks to reach the intensity of the average level, with its value typically ranging from 0 to 3. The detailed training process is summarized in Algorithm 2.

Algorithm 2.

Algorithm 2: Training with GradNorm

Initialize $w_i(0) = 1$, where $i = [1, 2, 3]$; Initialize network parameters p

for $t = 0$ **to** epoch **do**

Compute $L_i(t)$ and $L_{\text{total}}(t) = \sum_i w_i(t) L_i(t)$

Compute $G_{\text{p}}^{(i)}(t)$ and $r_i(t)$

Compute $\overline{G}_{\text{p}}(t)$ by averaging the $G_{\text{p}}^{(i)}(t)$

Compute $L_{\text{grad}}(t) = \sum_i (G_{\text{p}}^{(i)}(t) - \overline{G}_{\text{p}}(t) \times [r_i(t)]^{\alpha})$

Compute GradNorm gradients $\nabla_{w_i} L_{\text{grad}}(t)$, keeping targets $\overline{G}_{\text{p}}(t) \times [r_i(t)]^{\alpha}$ constant

Compute standard gradients $\nabla_{\text{p}} L_{\text{total}}(t)$

Update $w_i(t) \to w_i(t+1)$ using $\nabla_{w_i} L_{\text{grad}}(t)$

Update $\text{p}(t) \to \text{p}(t+1)$ using $\nabla_{\text{p}} L_{\text{total}}(t)$

Renormalize $w_i(t+1)$ so that $\sum_i w_i(t+1) = 3$

end for

2.6. Workflow and network architecture

The workflow of the BSFC-SSL method for AVO inversion consists of two parts: training and prediction. During the training phase, the BSFC-SSL method requires the simultaneous training of the forward-modeling network, the inversion network, and the BSFC network, thereby achieving closed-loop optimization among all three. Before starting the training, we initialize the weights and biases of the neural networks. The data include labeled, unlabeled seismic data, and well-log elastic parameters (P-wave velocity, S-wave velocity, and density). Additionally, a low-frequency model is integrated into the network, alongside the seismic data, as prior information. During the training process, both labeled and unlabeled seismic data are utilized to optimize the inversion and forward networks. The output of the forward network is fed back to the inversion network in the form of pseudo-labels, enabling the effective utilization of unlabeled data. Meanwhile, well-log elastic parameters contribute to the optimization of the inversion network, forward network, and BSFC network. Eventually, a mapping between multi-trace seismic data and multi-trace elastic parameters is achieved. During the prediction stage, the BSFC network and the forward network are no longer involved, and the inversion task is completed solely by leveraging the efficient inference capability of the inversion network.

This workflow is implemented through three core subnetworks with specifically designed architectures. The BSFC-SSL consists of three subnetworks: the inversion network, the forward network, and the bidirectional spatial feature constraints network. To accomplish the inversion task, we adopted the CNN as the basic architecture. Given the need to extract global features from the shallow structure in the inversion network, which requires a larger receptive field, we introduced TCN and a dilated convolution design. Dilated convolution allows for precise control of the receptive field by introducing a dilation factor, enabling the

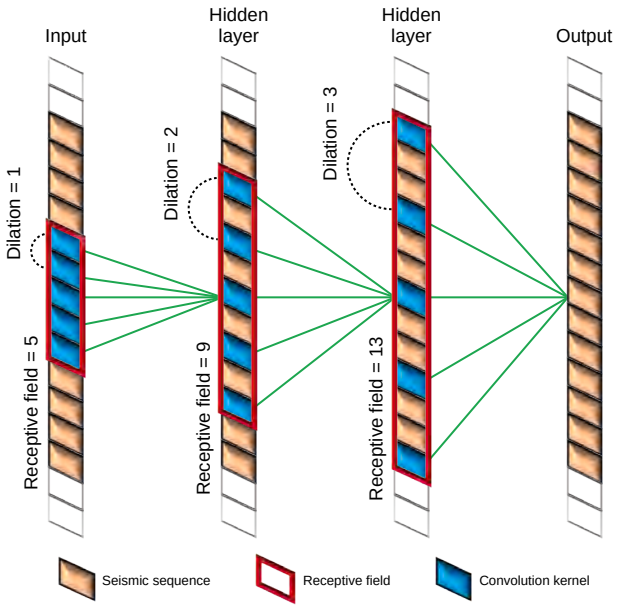

Fig. 4. The structure of dilated convolution.

network to achieve a larger receptive field with fewer layers, thereby capturing historical information over a longer time scale. Fig. 4 illustrates the structure of a 5 × 5 dilated convolution kernel. In this diagram, the orange blocks represent the seismic sequence, whereas the blue blocks indicate the convolution kernel, corresponding to an initial receptive field of 5. When dilation factors of 2 and 3 are applied, the receptive fields of a single-layer network expand to 9 and 13, respectively. The use of dilated convolution significantly enhances the network's ability to extract shallow global features while reducing the number of parameters. Fig. 5 illustrates the inversion network and forward network, consisting of four TCN blocks and three CNN blocks. Here, K is the number of seismic profiles corresponding to different incidence angles. The structure of the TCN, highlighted within the dashed box in Fig. 5, consists of two branches. The first branch transforms the input, while the second applies a 1 × 1 convolution operation. The outputs from both branches are then combined to produce the final result. The residual connection enables information to flow across layers, effectively mitigating information loss caused by excessive depth. It is worth noting that the architectures of our forward and inversion networks are consistent. Using the same network structure helps to avoid prediction bias or instability caused by architectural differences (Sang et al., 2023). The BSFC network employs CNN as its basic architecture because CNN has demonstrated remarkable advantages in seismic trace interpolation tasks, which are analogous to the feature recovery function of BSFC. Specifically, the convolutional layers of CNN can extract hierarchical spatial features from seismic data, and the shared weight mechanism and local receptive field structure enable efficient capture of spatial continuity in seismic profiles (Wang et al., 2020b, 2022a). As shown in Fig. 6, the architecture of the BSFC network consists of convolutional layers with 16 channels at both ends, and a central section composed of multiple convolutional layers. Given that the optimal number of network layers remains undetermined, the number of convolutional layers is treated as a hyperparameter. Each convolutional layer is sequentially followed by a batch normalization (BN) layer and a ReLU activation function.

3. Experiments

3.1. Performance metrics and hyperparameters

To quantify the accuracy of the inversion results, we introduced the Pearson correlation coefficient (PCC), coefficient of determination (R^2), and root mean square error (RMSE). PCC is a measure of the linear relationship between two variables, quantifying the strength and direction of their correlation. It is defined as

$$\mathrm{PCC} = \frac{\sum_{k=1}^{n}(m_k - \mu_m)(\widehat{m}_k - \mu_{\widehat{m}})}{\sqrt{\sum_{k=1}^{n}(y_k - \mu_m)^2}\sqrt{\sum_{k=1}^{n}(\widehat{m}_k - \mu_{\widehat{m}})^2}} \tag{18}$$

where m_k is the k-th true value, $\widehat{m}_k$ represents the k-th predicted value, μ_m and $\mu_{\widehat{m}}$ are the mean values of the input parameters and predicted values, respectively, and n denotes the number of data points. The R^2 score is a statistical indicator used to measure the prediction effect of a regression model, representing the degree to which the model explains the total variation of the target variable. Its value ranges from 0 to 1, and the closer the R^2 score is to 1, the closer the prediction results are to the true values. The definition of R^2 is

$$R^2 = 1 - \frac{\sum_{k=1}^{n}(m_k - \widehat{m}_k)^2}{\sum_{k=1}^{n}(m_k - \mu_m)^2} \tag{19}$$

The RMSE was obtained by taking the square root of the mean-square error (MSE), which is a measure of the difference between the predicted value and the true value. The RMSE can be formulated as

$$\mathrm{RMSE} = \sqrt{\frac{1}{n}\sum_{k=1}^{n}(m_k - \widehat{m}_k)^2} \tag{20}$$

For network training, we set a series of hyperparameters, as listed in Table 1. It is worth noting that the number M of multi-trace inputs is set to 17, the parameter α in Algorithm 2 is set to 1.2, and the number of internal convolutional layers of the BSFC network is 3. The settings of these hyperparameters are elaborated in detail in the discussion section. The experiment was conducted on a computer running the Windows 11 operating system, with a configuration that included 32 GB of RAM, an Intel Core i5-12490F processor, and an NVIDIA GeForce GTX 3060 graphics card with 8 GB of video memory. The experiments were conducted using the PyTorch framework.

3.2. Testing on Marmousi2 model

To verify the effectiveness of the BSFC-SSL method, we used the Marmousi2 model data for inversion tests. This model includes 2720 common depth points (CDPs) and 600 sampling points, with a sampling interval of 2 ms. Reflection coefficients were calculated from the model using Eq. (2) and convolved with a zero-phase Ricker wavelet of 20 Hz dominant frequency. As shown in Fig. 7(a)–(e), five sets of seismic data with incident angles ranging from 0° to 24° (at equal intervals) were

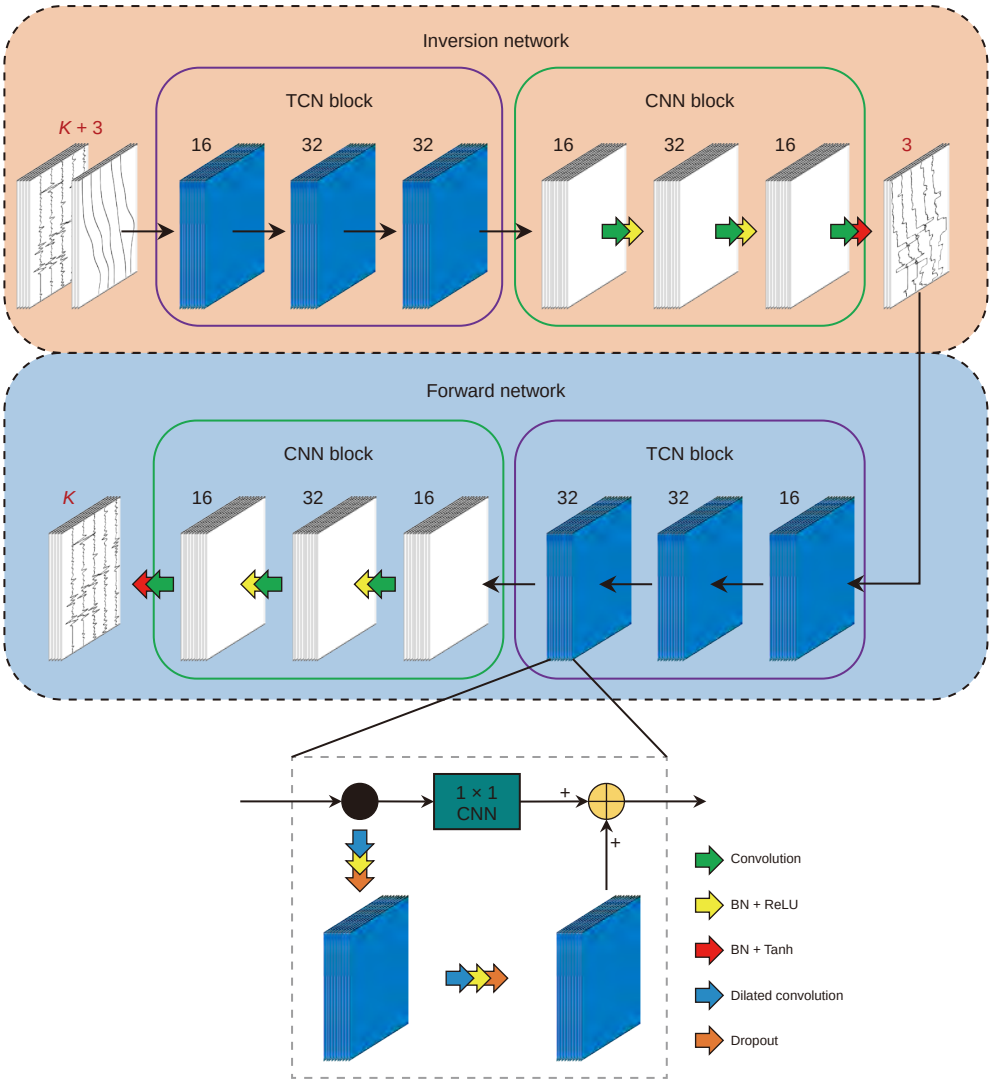

Fig. 5. Architectures of the inversion network and forward network.

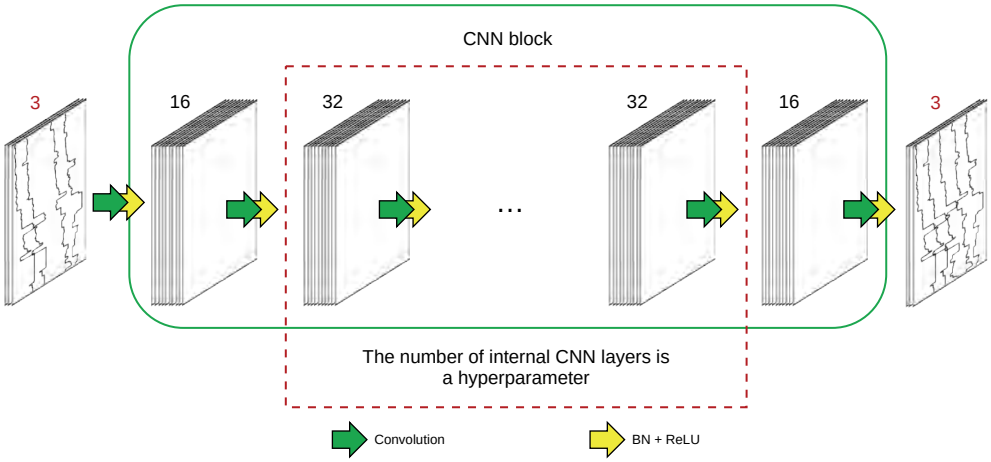

Fig. 6. Architecture of the BSFC network. The number of convolutional layers within the CNN block (enclosed in the red-dashed box) is treated as a hyperparameter.

synthesized as input. Additionally, a low-pass filter was applied to the model data to obtain the low-frequency model, which is shown in Fig. 7(f)–(h). As shown in Fig. 8, we extracted 18 traces at equal intervals to construct the labeled dataset, which accounted for only 0.66% of the total traces. The remaining traces were randomly sampled at an interval of 50 traces as the unlabeled data. Fig. 9 shows the loss curves of BSFC-SSL, and all losses can converge stably.

Table 1
Hyperparameters in BSFC-SSL.

The type of the hyperparameter		Value
Basic parameter	Epoch	500
	Batch size	60
	Learning rate	0.002
	Weight decay	0.0001
	Dropout	0.2
	Initial kernel size	3
	α in GradNorm	1.2
	Width M	17
Inversion network	Number of channels of TCN	[16,32,32,16]
	Dilation factor of TCN	[1,2,4,8]
	Number of channels of CNN	[32,16,3]
Forward network	Number of channels of TCN	[16,32,32,16]
	Dilation factor of TCN	[1,2,4,8]
	Number of channels of CNN	[32,16,5]
BSFC network	Number of internal CNN layers	3
	Number of channels of CNN	[16,32,32,32,16,3]

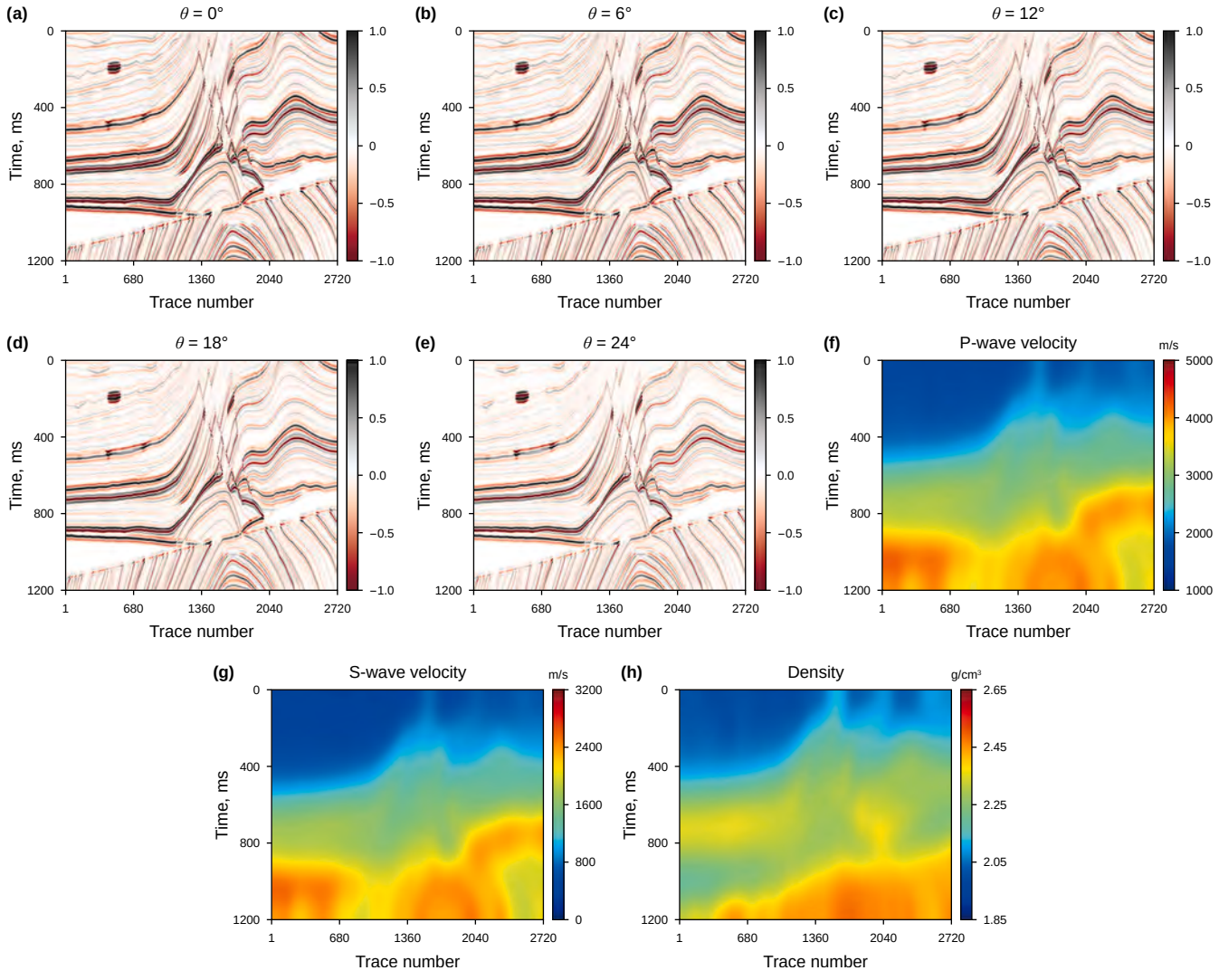

Fig. 7. Synthetic angle gather profiles with different incident angles of **(a)** 0°, **(b)** 6°, **(c)** 12°, **(d)** 18°, and **(e)** 24°. Low-frequency profile of **(f)** P-wave velocity, **(g)** S-wave velocity, and **(h)** density.

To evaluate the effectiveness of the proposed method, we compared it with a comprehensive suite of approaches. The compared methods included: one-dimensional methods, namely supervised learning (1D-SL) and semi-supervised learning (1D-SSL), which were constructed using the core architecture of our framework but limited to 1D convolutional operations and

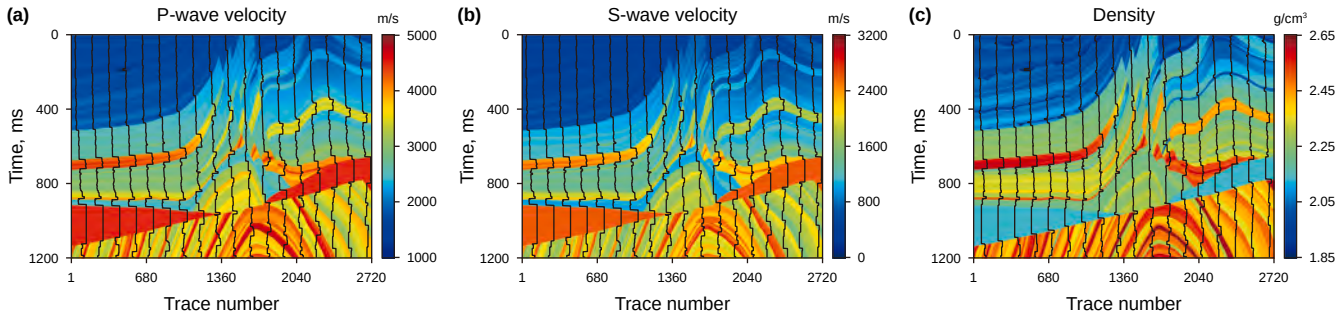

Fig. 8. Training traces of **(a)** P-wave velocity, **(b)** S-wave velocity, and **(c)** density.

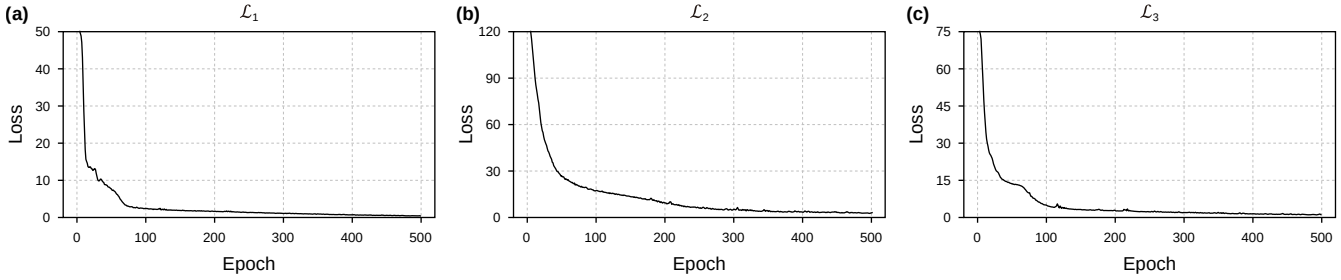

Fig. 9. Loss function curves of **(a)** $\mathscr{L}_1$, **(b)** $\mathscr{L}_2$, and **(c)** $\mathscr{L}_3$ for the synthetic data.

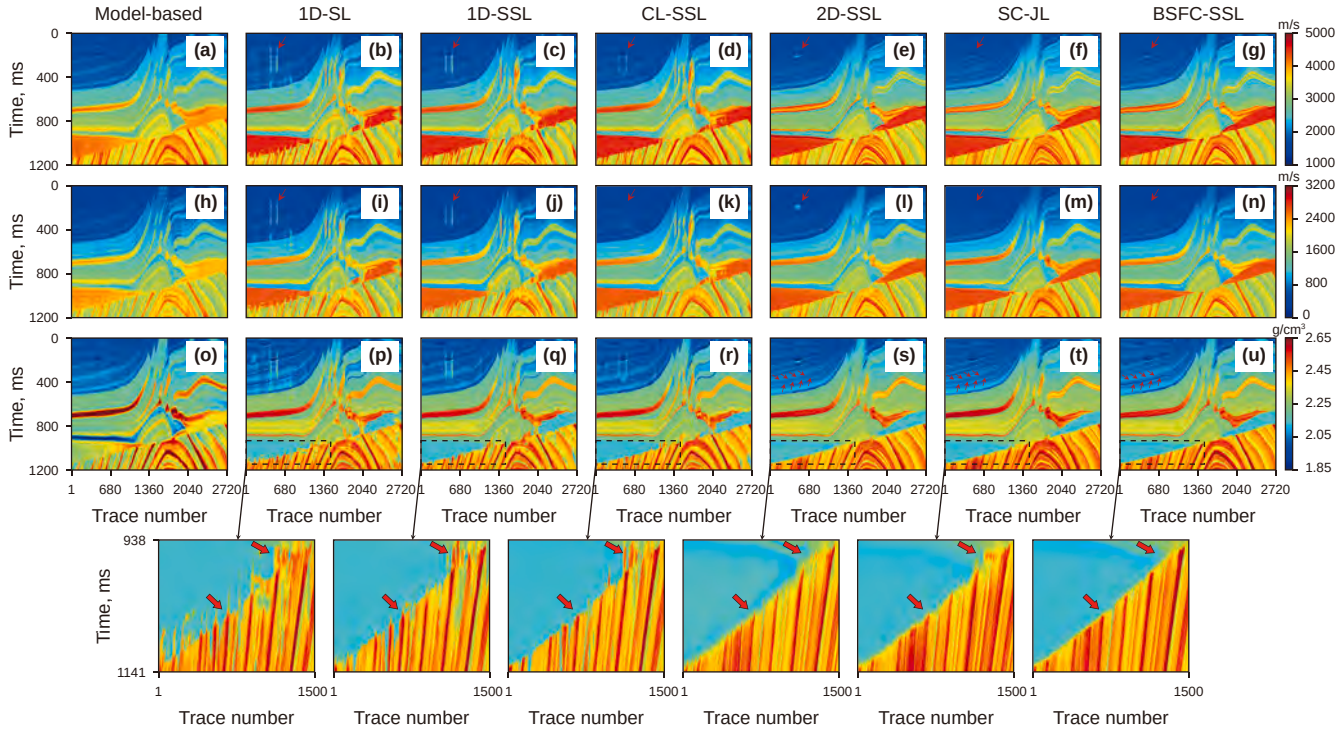

Fig. 10. Inversion results for **(a)**–**(g)** P-wave velocity, **(h)**–**(n)** S-wave velocity, and **(o)**–**(u)** density obtained using different methods. The first column presents the model-based inversion results, followed by the 1D-SL results in the second column, the 1D-SSL results in the third, the CL-SSL results in the fourth, the 2D-SSL results in the fifth, the SC-JL results in the sixth, and the BSFC-SSL results in the final column.

excluding the bidirectional constraints, with the CL-SSL (Shi et al., 2024) being introduced as a representative state-of-the-art method in this category; two-dimensional semi-supervised methods, including a standard implementation (2D-SSL), which adopts the same 2D network backbone as our method but without bidirectional spatial constraints, and the SC-JL (Mustafa et al., 2021) method as a strong baseline that explicitly leverages spatial information. Additionally, the widely used model-based method (L-BFGS) (Ahmed et al., 2022) was included as a benchmark. Fig. 10 shows the inversion results for various methods.

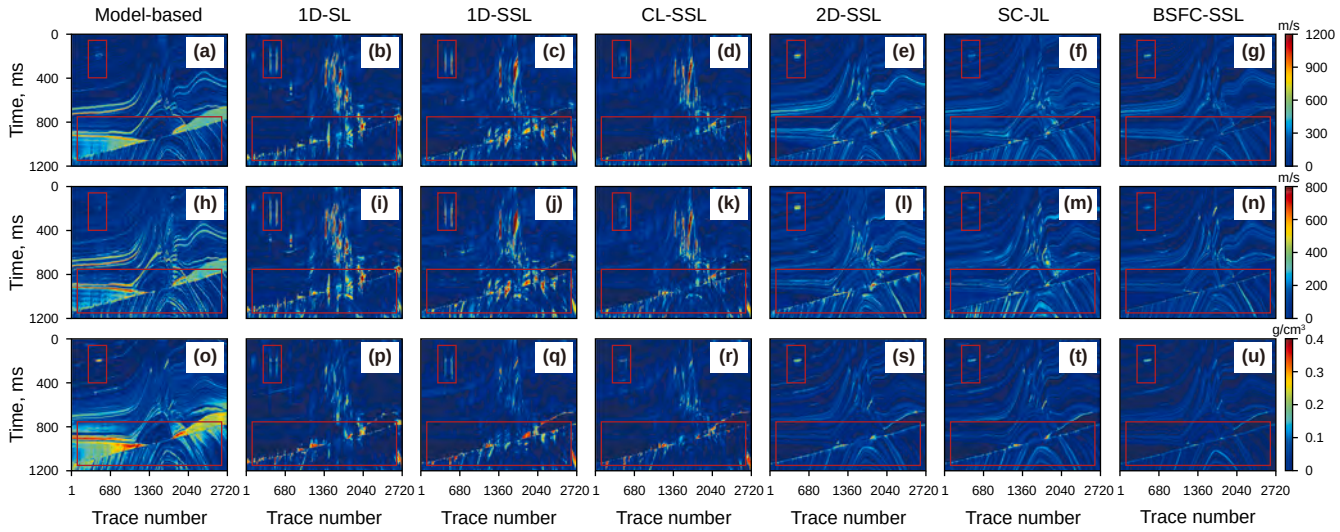

Fig. 11. Absolute difference in **(a)**–**(g)** P-wave velocity, **(h)**–**(n)** S-wave velocity, and **(o)**–**(u)** density inversion results compared to the true data. The figure layout is consistent with Fig. 10.

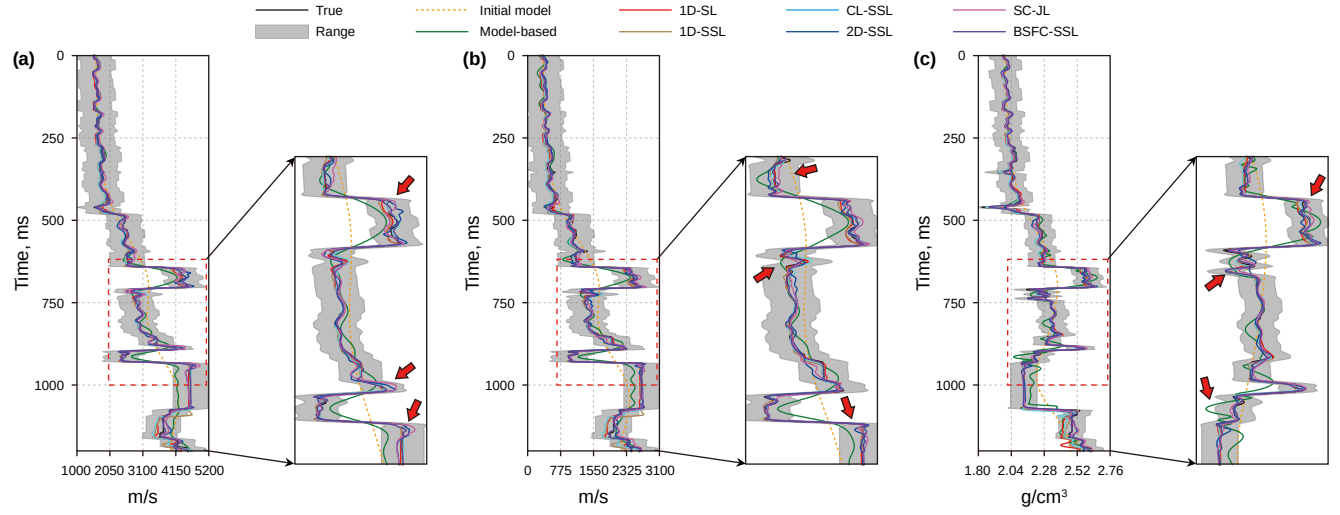

Fig. 12. Inversion results for **(a)** P-wave velocity, **(b)** S-wave velocity, and **(c)** density at trace 600 in the synthetic dataset. The black lines represent the true values, and the orange dotted lines denote the initial models. The gray shaded region indicates the standard deviation range of the true data. The green lines show the model-based inversion results, the red lines show the 1D-SL results, the brown lines show the 1D-SSL results, the sky-blue lines show the CL-SSL results, the blue lines show the 2D-SSL results, the pink lines show the SC-JL results, and the purple lines show the BSFC-SSL results.

Table 2
Quantitative analysis of the inversion results for the synthetic data.

Method	P-wave velocity			S-wave velocity			Density		
	PCC	R^2	RMSE	PCC	R^2	RMSE	PCC	R^2	RMSE
Model-based	0.9731	0.9447	0.0757	0.9715	0.9402	0.1291	0.8478	0.6754	0.0437
1D-SL	0.9694	0.9173	0.0774	0.9682	0.9147	0.1285	0.9495	0.8834	0.0229
1D-SSL	0.9786	0.9467	0.0654	0.9775	0.9442	0.1093	0.9597	0.9049	0.0215
CL-SSL	0.9814	0.9587	0.0603	0.9786	0.9534	0.0977	0.9653	0.9211	0.0194
2D-SSL	0.9863	0.9669	0.0553	0.9846	0.9637	0.0832	0.9751	0.9403	0.0166
SC-JL	0.9879	0.9712	0.0536	0.9867	0.9654	0.0805	0.9775	0.9461	0.0159
BSFC-SSL	**0.9911**	**0.9814**	**0.0420**	**0.9892**	**0.9779**	**0.0624**	**0.9868**	**0.9617**	**0.0123**

While model-based methods can effectively display the stratigraphic structure, their resolution tends to be relatively lower. The 1D-SL method improves inversion resolution but brings noticeable vertical artifacts. Although the 1D-SSL and CL-SSL methods reduce these artifacts to some degree, they are still blurred at the rock layer unconformities, as shown by the elliptical wireframes in Fig. 10. The 2D-SSL, SC-JL, and BSFC-SSL methods improve lateral continuity in the inversion results. Compared to the 2D-SSL and SC-JL methods, the BSFC-SSL method offers clearer delineation at the boundaries of thin layers (red arrows, Fig. 10(s)–(u)). Fig. 11

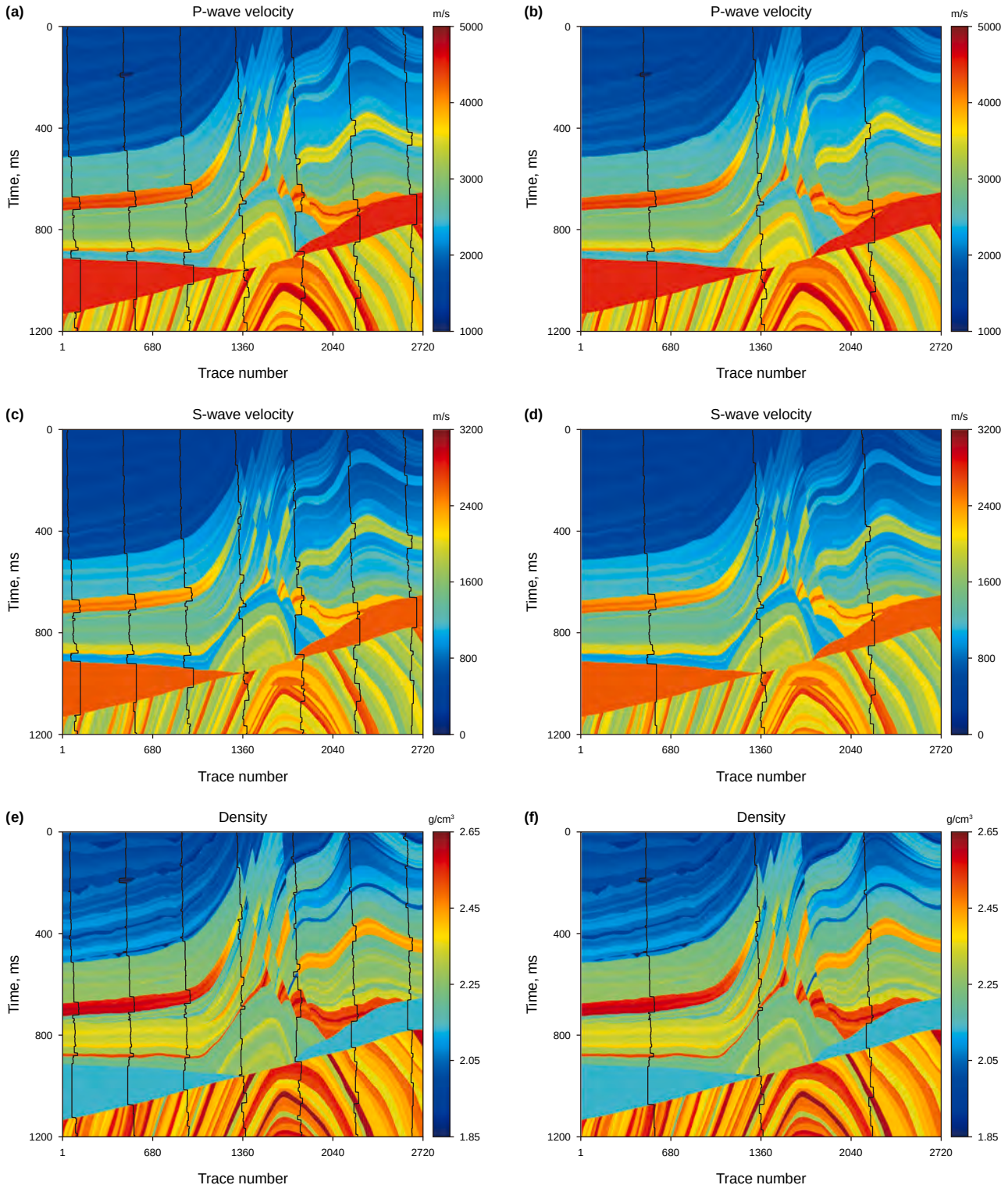

Fig. 13. **(a)** Seven training traces and **(b)** three training traces for P-wave velocity; **(c)** seven training traces and **(d)** three training traces for S-wave velocity; **(e)** seven training traces and **(f)** three training traces for density.

shows the residuals between the inversion results of each method and the true values. The BSFC-SSL method exhibits low errors in both the reservoir and complex geological structures (red rectangular boxes). Fig. 12 shows the prediction results for trace 600 not included in the training data. A comparison of the inversion results with the measured single trace clearly demonstrates that the BSFC-SSL method produces more accurate results (as indicated by the red arrow). Despite the extreme complexity of the structural features and significant lithological changes at depths of 620 ms, the inversion results using the BSFC-SSL method maintain high accuracy. To quantitatively compare the accuracy of each method, we calculated the mean values of the inversion profiles using PCC,

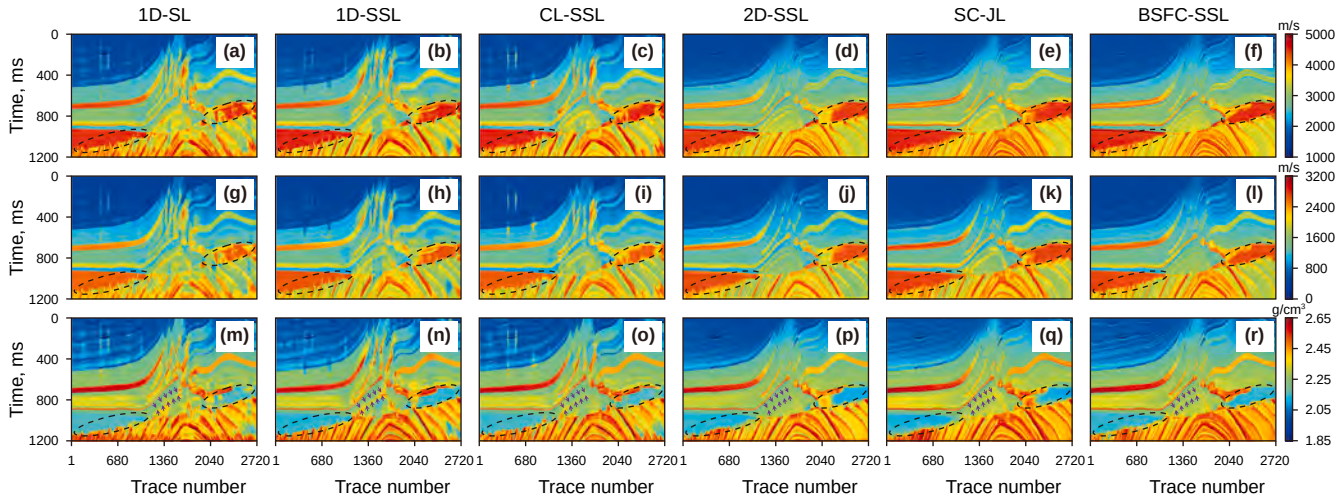

Fig. 14. Inversion results for **(a)**–**(f)** P-wave velocity, **(g)**–**(l)** S-wave velocity, and **(m)**–**(r)** density obtained using different methods with seven training traces. The first column presents the 1D-SL inversion results, followed by the 1D-SSL results in the second column, the CL-SSL results in the third, the 2D-SSL results in the fourth, the SC-JL results in the fifth, and the BSFC-SSL results in the final column.

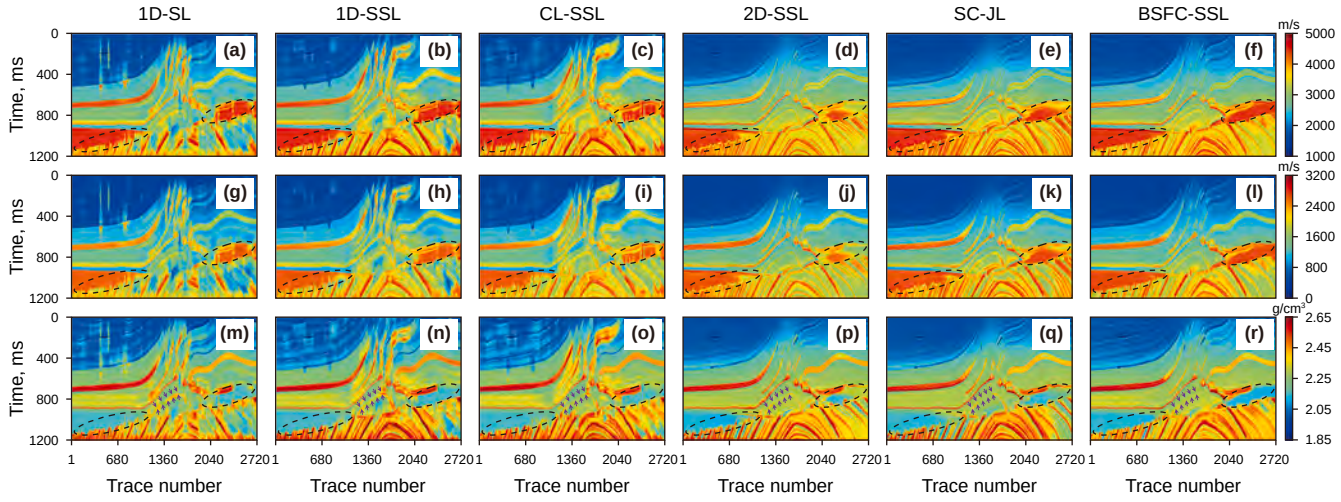

Fig. 15. Inversion results for **(a)**–**(f)** P-wave velocity, **(g)**–**(l)** S-wave velocity, and **(m)**–**(r)** density obtained using different methods with three training traces. The figure layout is consistent with Fig. 14.

R^2, and RMSE. The results, listed in Table 2, demonstrate that the BSFC-SSL method outperforms all other methods, achieving the best values across all indicators.

In practical applications, the number of available well-log labels is often limited due to complex geological conditions and high well-log costs. Therefore, we further designed a comparison of various methods under the condition of scarce labels. As shown in Fig. 13, we sampled seven and three training traces at equal intervals, which represent only 0.26% and 0.11% of the total number of traces, respectively. Figs. 14 and 15 show the inversion results using seven and three training traces, respectively. As the number of training traces decreases, the vertical artifacts of the 1D-SL, 1D-SSL, and CL-SSL methods become significantly more severe. Although the 2D-SSL and SC-JL methods improve lateral continuity, they still exhibit numerous high-value errors in complex strata (see the areas marked by the elliptical box). In contrast, the BSFC-SSL method maintains high accuracy and resolution by fully considering the relationships between adjacent traces. Fig. 16 shows the quantitative comparison of different inversion methods. By comparison, we can see that the BSFC-SSL method achieves higher PCC and R^2 values, along with a low RMSE. This verifies the efficiency and accuracy of the proposed method under limited well-log labels.

The robustness of an inversion method to noise is another critical concern in seismic exploration, as data are often contaminated, which can degrade the accuracy of inversion results (Li et al., 2022b). To evaluate the noise robustness of the proposed method, we conducted additional inversion experiments on the synthetic Marmousi2 dataset. Following the same configuration as in Fig. 10, which used 18 equally spaced traces as well-log labels, we added a 1:1 mixture of random and colored noise to the clean seismic data to achieve different signal-to-noise ratios (SNRs: 2, 5, 10, and 20 dB). Fig. 17(a)–(d) show the 0°-incident-angle seismic profiles at these SNR levels. To intuitively illustrate the noise intensity, a randomly selected seismic trace is displayed in Fig. 17(e), showing the corresponding waveforms at various SNRs. The inversion results of the BSFC-SSL method for these datasets are presented in Fig. 18. Both qualitative and quantitative analyses

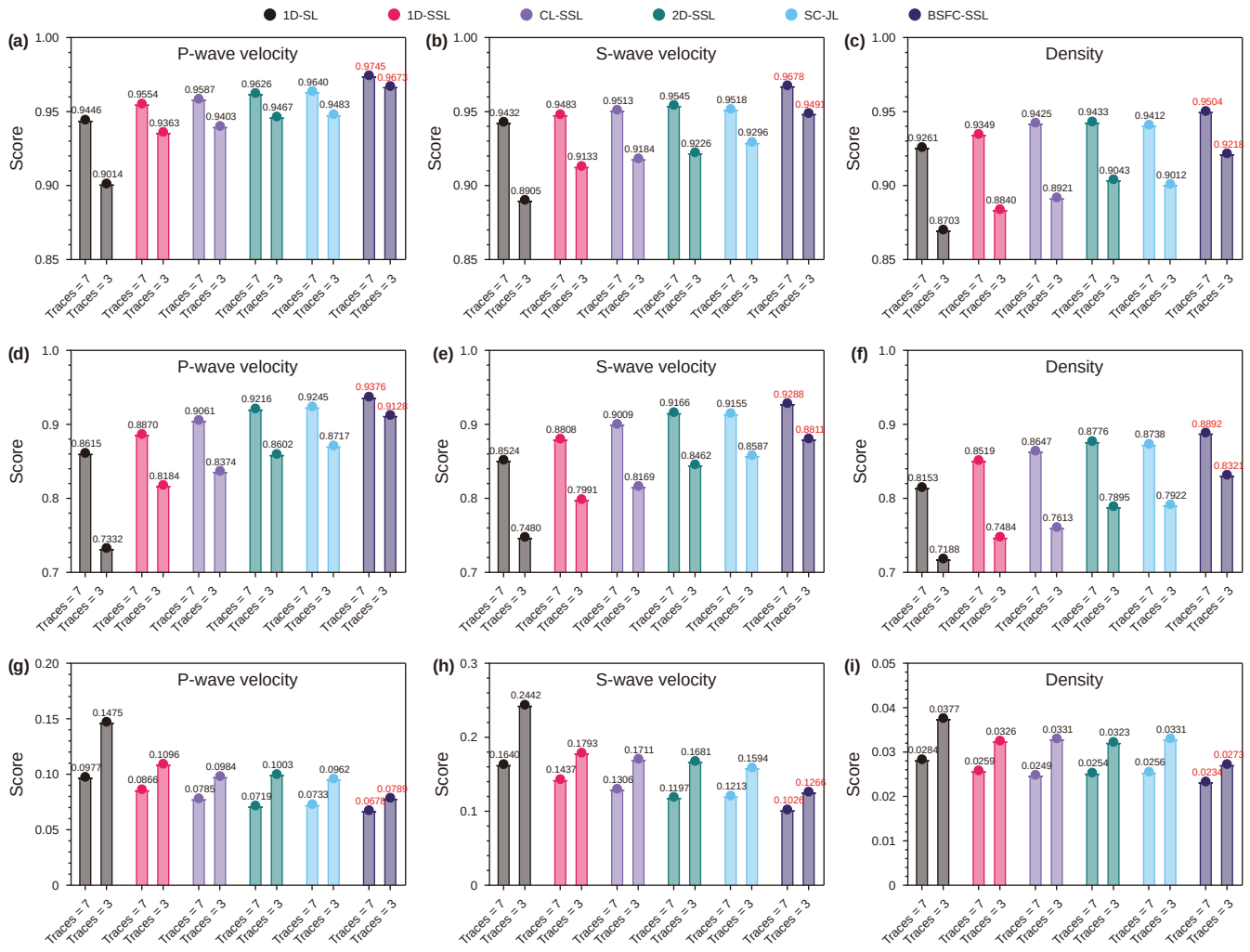

Fig. 16. Comparison of the **(a)**–**(c)** PCC, **(d)**–**(f)** R^2, and **(g)**–**(i)** RMSE of the different methods.

demonstrate that the proposed method maintains high inversion accuracy and stability across different noise levels, confirming its strong noise resistance.

3.3. Testing on field data

To verify the practicality of the BSFC-SSL method, we applied it to field data from the South China Sea. The main rock types in the field data are sandstone and mudstone, which feature complex lithology, significant thickness variations, and strong heterogeneity. Therefore, high accuracy and resolution of velocity and density are essential. We selected a line consisting of 630 common depth points (CDPs), passing through well G1 (CDP = 98), well G2 (CDP = 304), well G3 (CDP = 443), and well G4 (CDP = 615). Wells G1, G3, and G4 were used for training, while well G2 was used to evaluate the inversion results. Before inversion, the seismic data were processed using noise suppression, surface-consistent deconvolution, amplitude recovery, and resampling to improve the signal-to-noise ratio and resolution. The low-frequency information of the different elastic parameters is obtained by layer interpolation, extrapolation, and smoothing of the corresponding well-log curves. Fig. 19 shows the angle gather profiles and the low-frequency profiles. The hyperparameters were the same as those used in the synthetic data experiments. Fig. 20 shows the loss curves of the BSFC-SSL method for field data, including $\mathscr{L}_1$, $\mathscr{L}_2$, and $\mathscr{L}_3$. As training progresses, all losses decrease steadily and converge to stable low values. Fig. 21 displays the inversion results of the BSFC-SSL method at the training well locations (G1, G3, and G4), demonstrating a close match between the predicted and true well-log curves. These results further confirm the accuracy and reliability of the proposed method across multiple well locations in the field.

We performed AVO inversion on field data using the model-based, 1D-SL, 1D-SSL, CL-SSL, 2D-SSL, SC-JL, and BSFC-SSL methods, and the results are shown in Figs. 22–24. The model-based method, along with conventional DL-based and CL-SSL approaches, can effectively recover the primary stratigraphic features. However, these methods exhibit limited resolution, particularly in terms of accurately reconstructing density. Among the compared methods, the 2D-SSL and SC-JL approaches yield improved lateral continuity, yet the elastic parameters obtained using the BSFC-SSL method exhibit even higher resolution and more consistent lateral continuity, as indicated by the elliptically labeled regions. To achieve a further comparison, the model-based method and the DL-based method results at the location of the blind well G2 are shown in Fig. 25. Table 3 shows the PCC, R^2, and RMSE values between the inversion results at the well G2 and the well-log curves. The inversion results of BSFC-SSL can fit the well-log curves well, especially in the area indicated by the arrows.

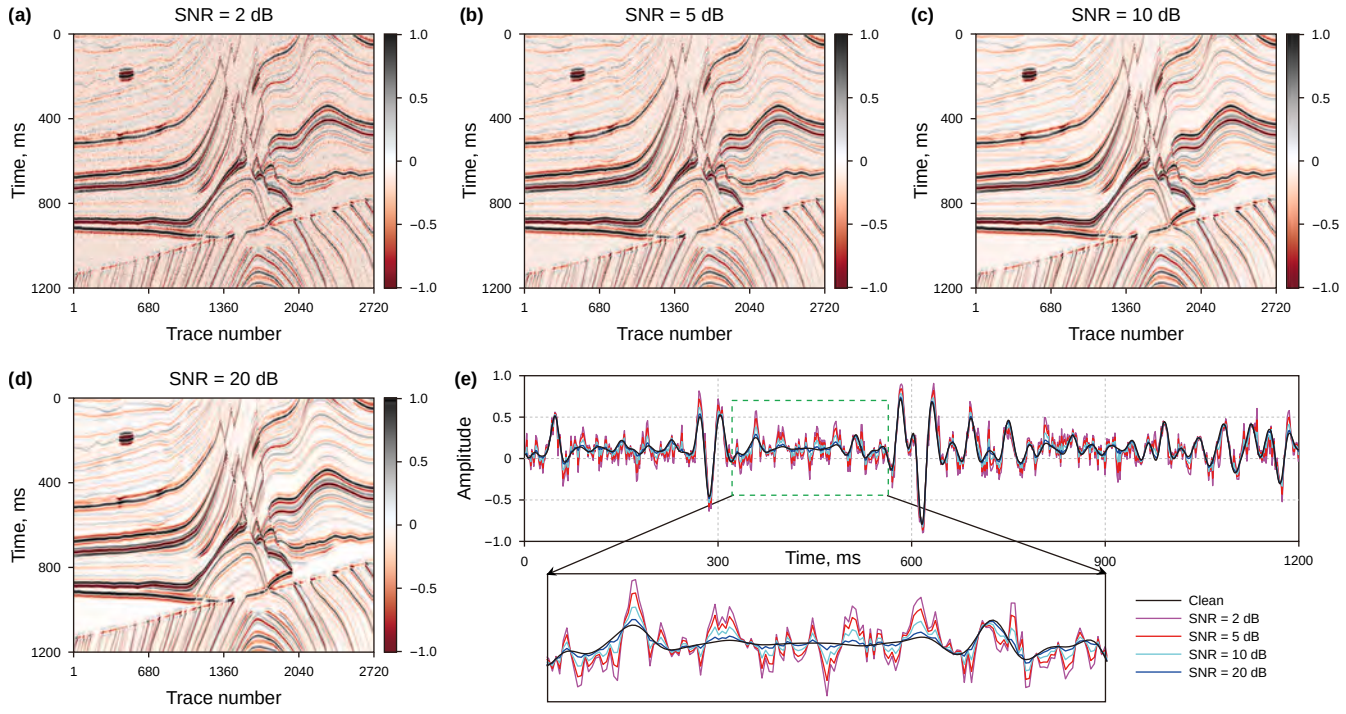

Fig. 17. Seismic profiles with 0° incident angle under different SNRs. **(a)** SNR = 2 dB. **(b)** SNR = 5 dB. **(c)** SNR = 10 dB. **(d)** SNR = 20 dB. **(e)** Waveform diagram of a randomly extracted seismic trace.

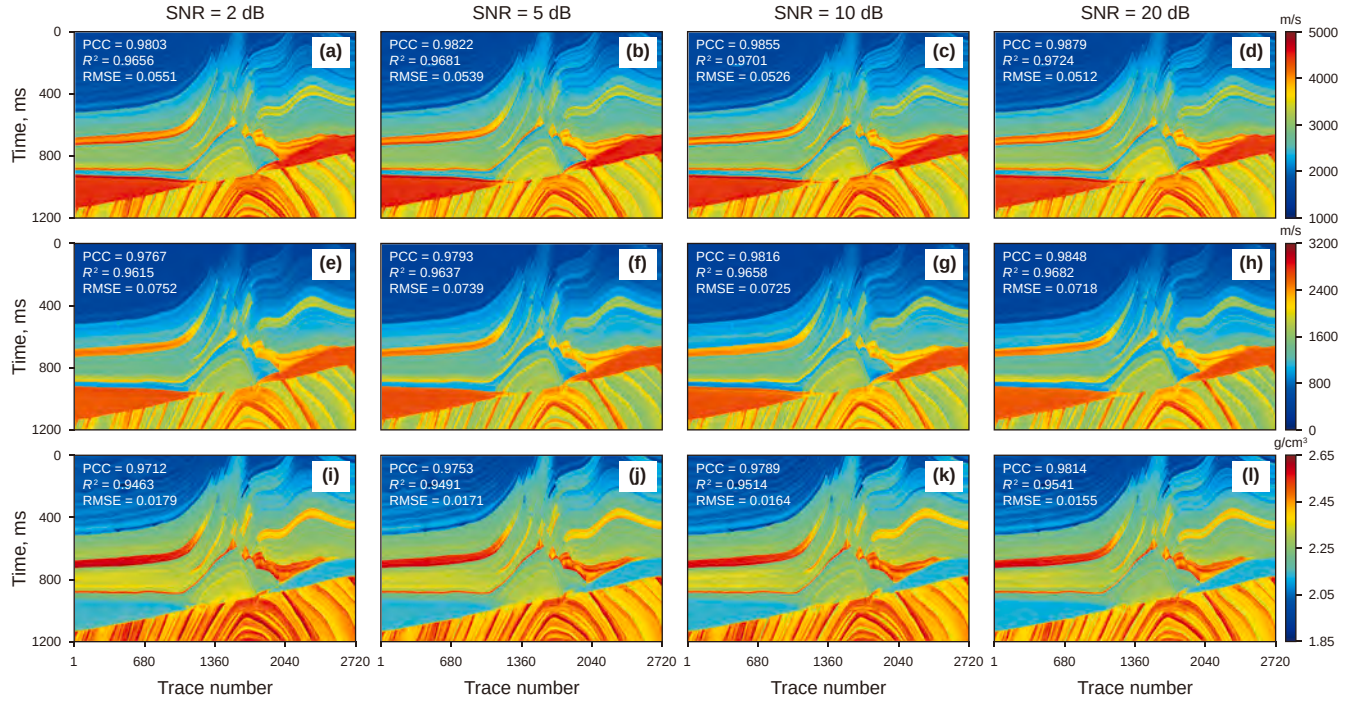

Fig. 18. BSFC-SSL inversion results of P-wave velocity, S-wave velocity, and density on synthetic data under different SNRs. **(a)**–**(d)** P-wave velocity; **(e)**–**(h)** S-wave velocity; **(i)**–**(l)** density. First column: SNR = 2 dB; second column: SNR = 5 dB; third column: SNR = 10 dB; last column: SNR = 20 dB. The evaluation score of each inversion result is displayed in the top-left corner of the corresponding subfigure.

4. Discussion

As a novel AVO inversion approach, BSFC-SSL incorporates a label annihilation operator and a bidirectional spatial feature constraint network. This method provides a new solution to the challenges of lateral continuity and efficient utilization of well-log data that commonly affect traditional deep learning-based AVO inversion techniques. It demonstrates enhanced performance in

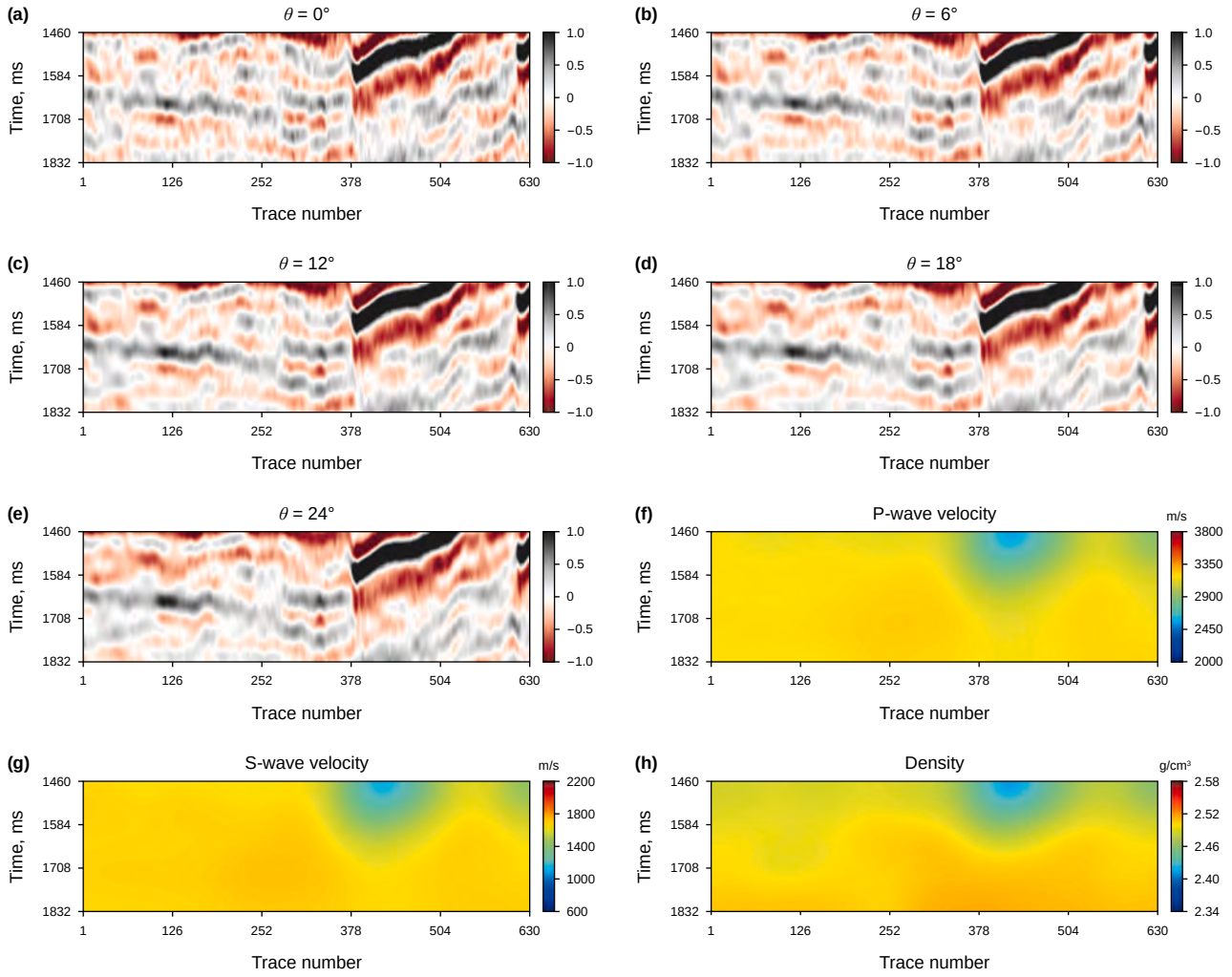

Fig. 19. Field seismic profiles of **(a)** 0°, **(b)** 6°, **(c)** 12°, **(d)** 18°, and **(e)** 24°. Low-frequency profile of **(f)** P-wave velocity, **(g)** S-wave velocity, and **(h)** density.

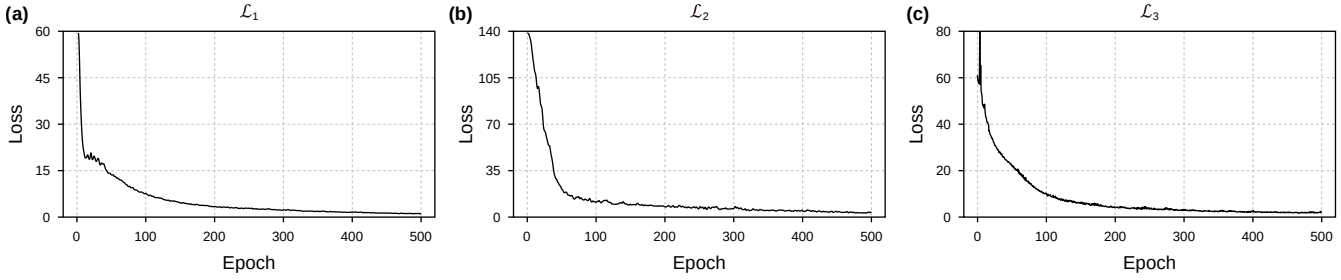

Fig. 20. Loss function curves of **(a)** $\mathscr{L}_1$, **(b)** $\mathscr{L}_2$, and **(c)** $\mathscr{L}_3$ for the field data.

both synthetic and field data experiments. Despite these promising results, several critical aspects of the BSFC-SSL framework warrant further investigation.

4.1. Inversion network structures comparison

In this article, the inversion network architecture of BSFC-SSL consists of four TCN layers and four CNN layers. This design was not chosen arbitrarily, but was informed by a series of considerations and empirical evaluations. To rigorously validate the effectiveness of the selected architecture, we conducted a supervised learning comparison using 18 seismic traces. Specifically, the four TCN layers were individually replaced with four CNN layers, four GRU layers, and four Transformer layers, and the inversion results were obtained through supervised learning. As shown in Fig. 26, the TCN-based architecture yields higher PCC and R^2, along with lower RMSE, for the inverted parameter profiles (P-wave velocity, S-wave velocity, and density). These experimental results strongly support the proposed network design.

4.2. Impact of α and BSFC network's convolutional layers

The hyperparameter α and the number of convolutional layers in the BSFC network are pivotal to the performance of the BSFC-SSL

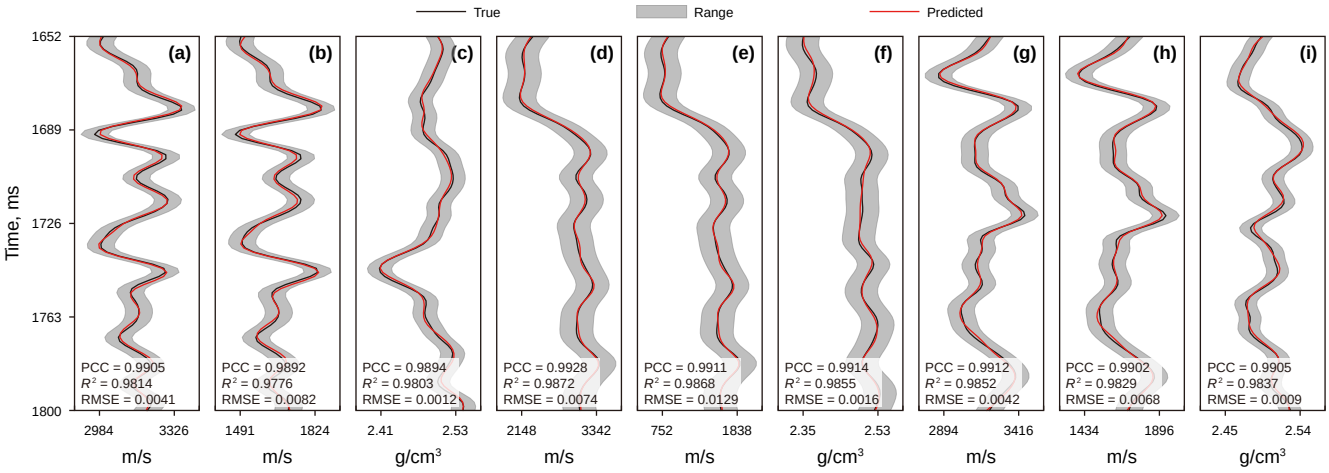

Fig. 21. Inversion results for three parameters at **(a)**–**(c)** well G1, **(d)**–**(f)** well G3, and **(g)**–**(i)** well G4. The black lines represent the true data, the gray shaded regions denote the standard deviation range of the true data, and the red lines show the BSFC-SSL inversion results. The evaluation score of each inversion result is displayed in the upper-left corner of the corresponding subfigure.

method, as they fundamentally govern the optimization dynamics and the model's capacity for spatial feature learning, respectively. Theoretically, α in the GradNorm strategy controls the intensity of balancing among the loss terms. An optimal α promotes concurrent learning across tasks, enhancing model stability and generalization. Our empirical results (Fig. 27) align with these expectations and crucially demonstrate the practical robustness of the method to this hyperparameter. The total loss ($\mathscr{L}_{\text{total}}$) decreases as α increases from 0 to 1.2, confirming that appropriate gradient normalization is essential. More importantly, the loss remains consistently low and stable across a range of values around this optimum (e.g., $\alpha \in [1.0, 1.5]$), indicating that the method is not overly sensitive to the precise setting of α. This robustness is a key advantage for field data applications, where exhaustive hyperparameter search is often impractical. Only when α exceeds a critical threshold (approximately 2.2) does overconstraining of gradient norms lead to the predicted training instability and performance degradation. Similarly, the number of convolutional layers determines the representational capacity of the BSFC network. Insufficient depth may limit the ability to capture essential bidirectional spatial dependencies, while excessive depth increases the risk of overfitting. Our analysis indicates that a three-layer architecture provides a stable and effective configuration for spatial feature learning. The interaction between network depth and α is moderated by model capacity: shallower networks (e.g., two layers) exhibit greater sensitivity to variations in α, whereas deeper networks show more consistent behavior. Overall, a three-layer BSFC network with $\alpha = 1.2$ achieves an optimal balance, offering a practical and robust guideline for model design and hyperparameter selection.

4.3. Determination of width M

In training the BSFC-SSL method, the width parameter M, which defines the number of adjacent traces incorporated alongside the input well-log data, significantly influences the inversion results. We conducted a series of experiments by incrementally increasing M from 3 to 23. For each value, we recorded both the training duration and the final total loss ($\mathscr{L}_{\text{total}}$) after convergence. As shown in Fig. 28, a clear trend was observed: increasing M consistently reduced $\mathscr{L}_{\text{total}}$, indicating that incorporating more neighboring traces enables the model to capture spatial information better and improve parameter estimation. Notably, the performance gains exhibit a plateau effect for $M > 13$, with marginal improvements beyond this point. This indicates that the method is not overly sensitive to the precise value of M in practical applications, as long as a sufficient spatial context (e.g., $M \geq 13$) is provided. This robustness is valuable when applying the method to field datasets with varying spatial characteristics. While the improvement in $\mathscr{L}_{\text{total}}$ comes at the cost of longer training times due to higher computational demands, the choice of $M = 17$ offers an optimal balance between accuracy and efficiency for our experimental setup. Nonetheless, the observed plateau indicates that practitioners may flexibly adjust M according to data availability or computational constraints without substantially compromising inversion quality.

4.4. Impact of well-log location

In this paper, we initially assumed that all wells were located in the middle trace, meaning that when using multi-trace input to the network, the number of traces around the well-log was the same. However, to explore a more comprehensive range of scenarios, we also investigated cases where the well-log location was not in the middle. With a fixed width $M = 17$, we varied the offset of the well-log position. The corresponding experimental results are shown in Fig. 29. An offset of 0 indicates that the well-log is exactly centered within the input window. Negative and positive offsets correspond to the well-log being shifted to the left and right, respectively. When the well-log location is close to the middle (offset close to 0), the total training loss is at its lowest. This is because when the well-log is in the middle, the network can more evenly utilize the surrounding trace information for training. Conversely, when the well-log location moves away from the middle (larger absolute values of offset), the total training loss increases. It is important to note that, compared to the influence of network structure and width M, the impact of well-log location on the training loss is relatively minor. This indicates that while well-

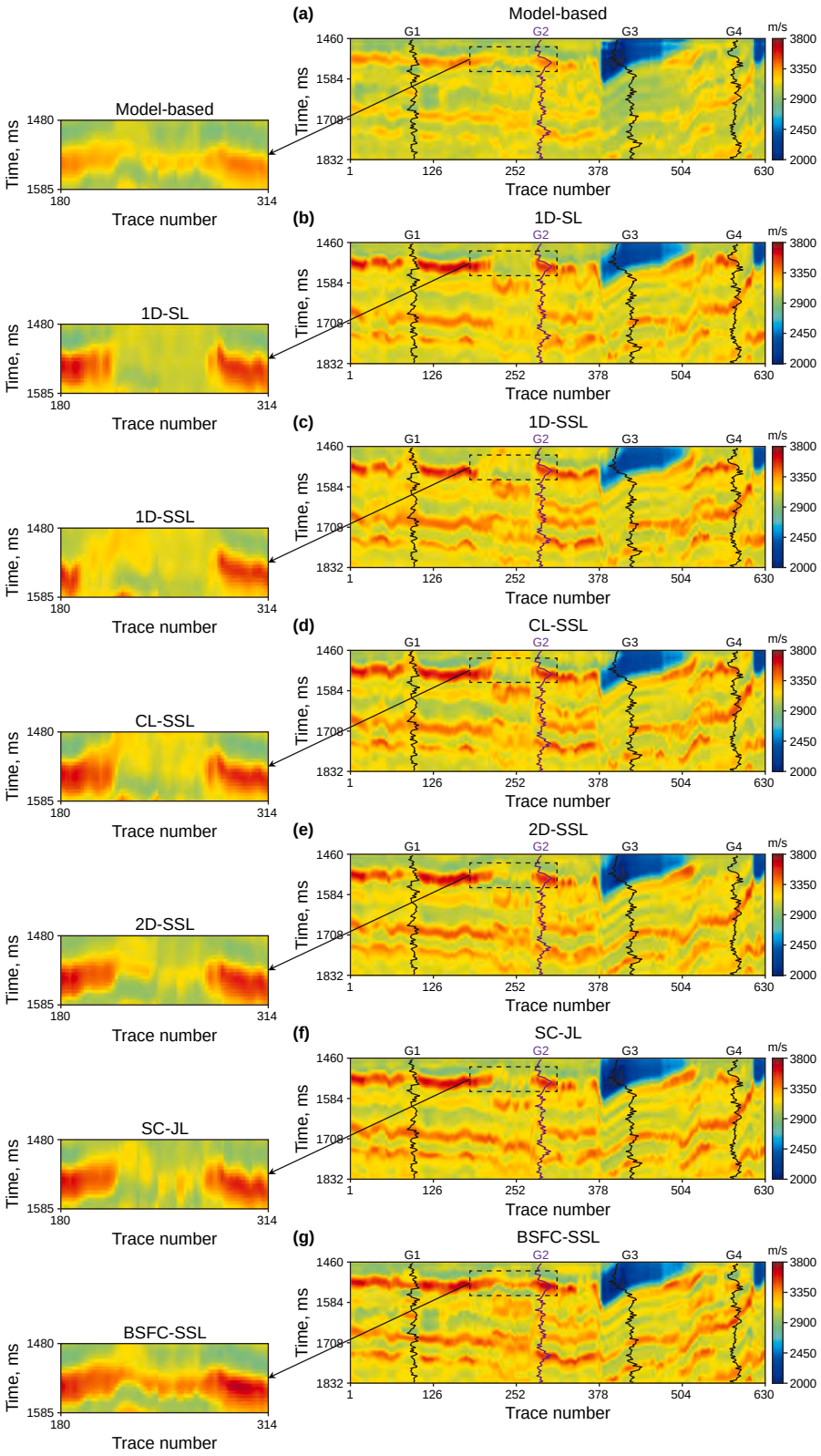

Fig. 22. Inversion results for P-wave velocity using **(a)** model-based, **(b)** 1D-SL, **(c)** 1D-SSL, **(d)** CL-SSL, **(e)** 2D-SSL, **(f)** SC-JL, and **(g)** BSFC-SSL methods.

log location does have an effect on the performance of the BSFC-SSL method, optimizing the network structure and appropriately selecting the width M are more critical factors in achieving accurate AVO inversion results.

4.5. Impact of the low-frequency model

The low-frequency model serves as critical prior information in seismic inversion, providing essential background trends that

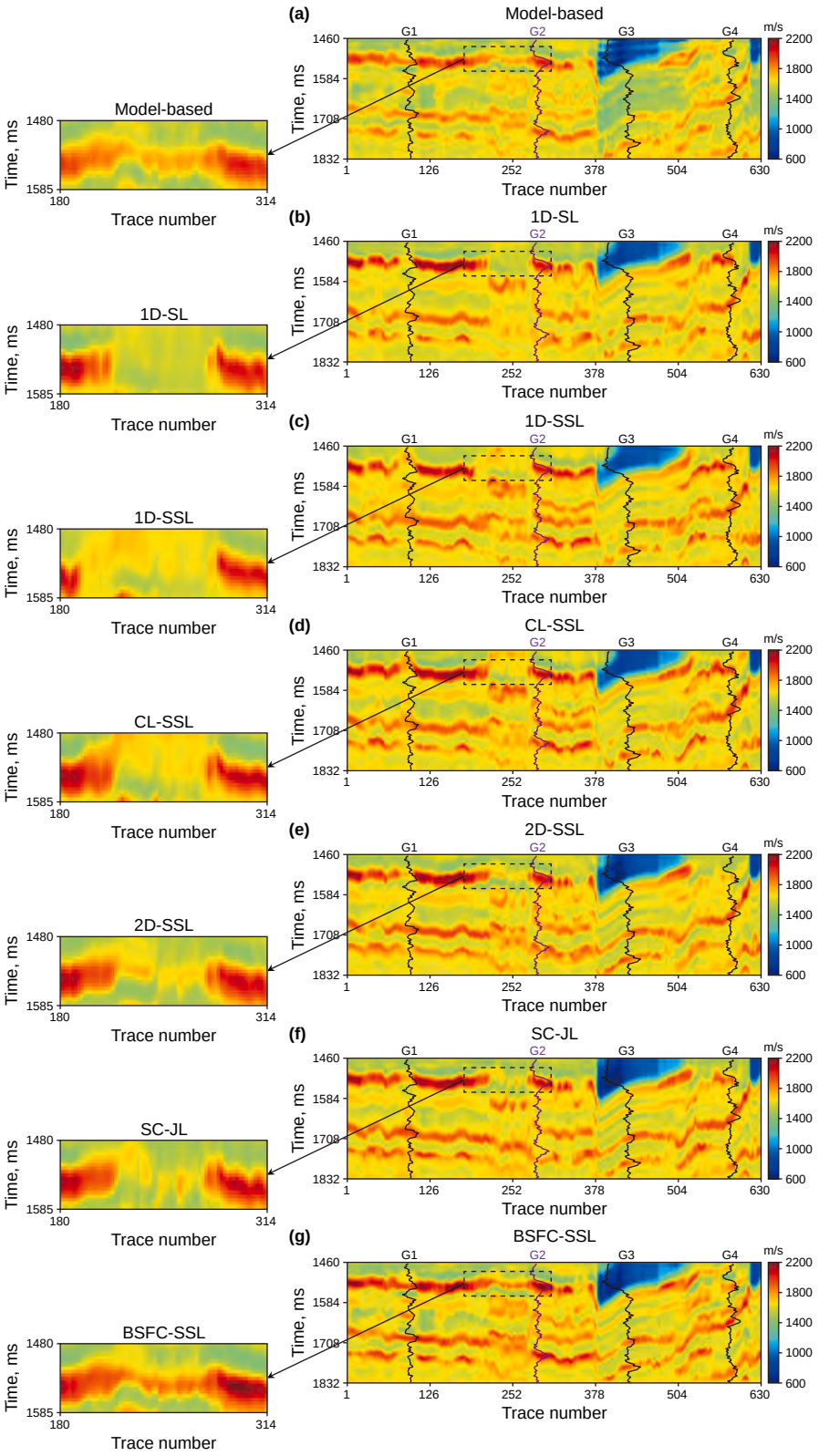

Fig. 23. Inversion results for S-wave velocity using **(a)** model-based, **(b)** 1D-SL, **(c)** 1D-SSL, **(d)** CL-SSL, **(e)** 2D-SSL, **(f)** SC-JL, and **(g)** BSFC-SSL methods.

compensate for the band-limited nature of seismic data. The quality and completeness of this model are pivotal for stabilizing ill-posed inverse problems and reducing solution non-uniqueness. To quantitatively evaluate the sensitivity of our BSFC-SSL framework to this input, we conducted a dedicated analysis. We designed a set of experiments using the Marmousi2 model, from which low-frequency components were extracted at 1 Hz intervals within the 1–5 Hz band. This approach yielded five distinct low-

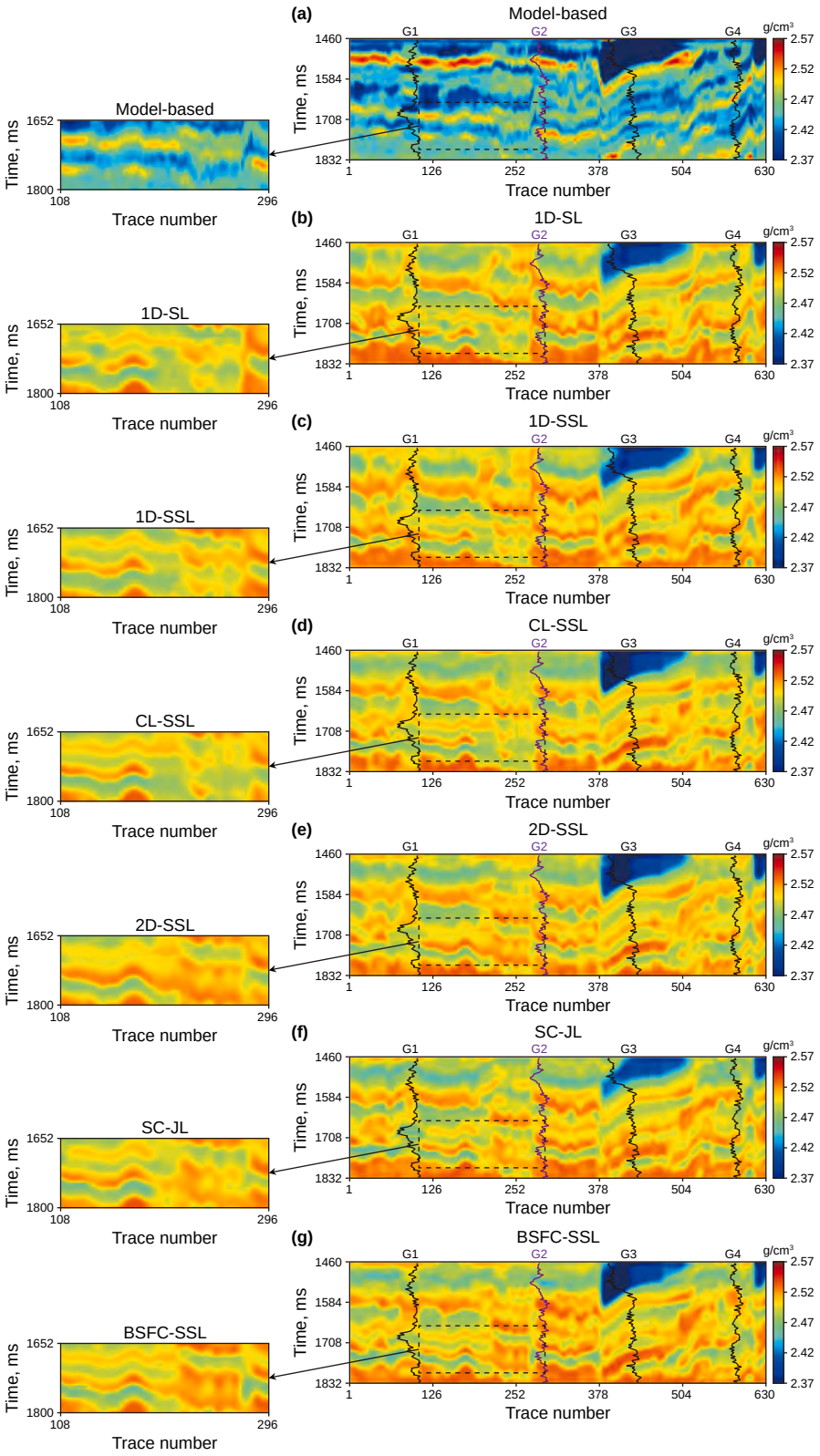

Fig. 24. Inversion results for density using **(a)** model-based, **(b)** 1D-SL, **(c)** 1D-SSL, **(d)** CL-SSL, **(e)** 2D-SSL, **(f)** SC-JL, and **(g)** BSFC-SSL methods.

frequency models, simulating a systematic gradient in the quality and richness of low-frequency information. In this context, the 5 Hz model represents the richest and most accurate scenario, while the 1 Hz model corresponds to the most sparse and challenging case. Fig. 30(a) illustrates the P-wave velocity of these low-frequency models at trace 100, and the evolution of the total loss during training is shown in Fig. 30(b). The experimental results confirm a consistent and monotonic trend: inversion

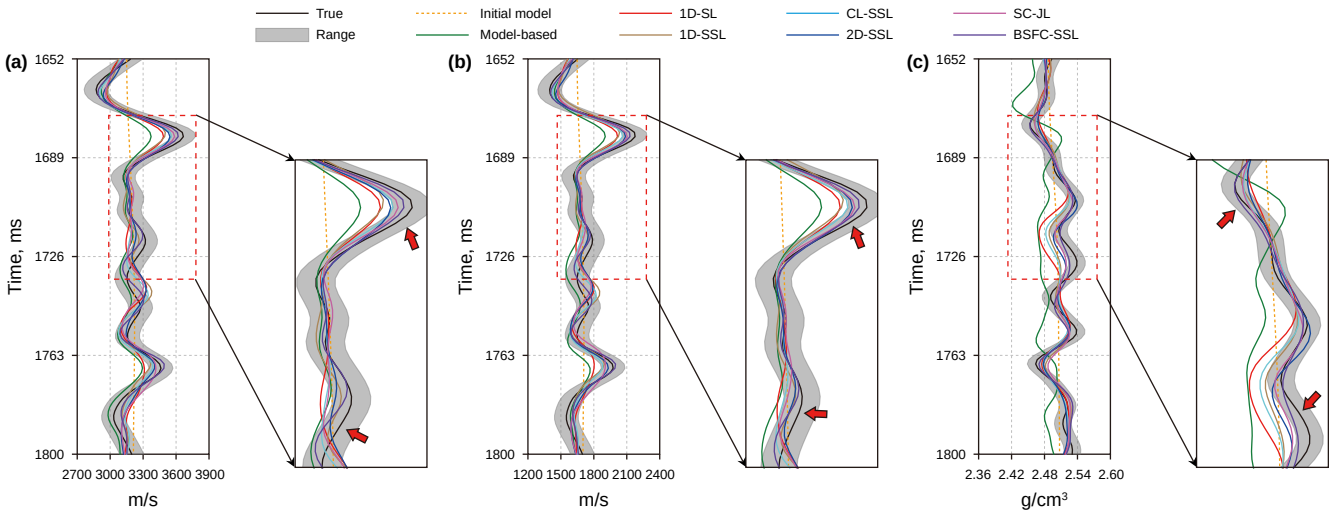

Fig. 25. Inversion results for **(a)** P-wave velocity, **(b)** S-wave velocity, and **(c)** density at well G2. The black lines represent the true values, and the orange dotted lines denote the initial models. The gray shaded region indicates the standard deviation range of the true data. The green lines show the model-based inversion results, the red lines show the 1D-SL results, the brown lines show the 1D-SSL results, the sky-blue lines show the CL-SSL results, the blue lines show the 2D-SSL results, the pink lines show the SC-JL results, and the purple lines show the BSFC-SSL results.

Table 3
Quantitative analysis of the inversion results for the field data.

Method	P-wave velocity			S-wave velocity			Density		
	PCC	R^2	RMSE	PCC	R^2	RMSE	PCC	R^2	RMSE
Model-based	0.7979	0.7582	0.0348	0.7512	0.6948	0.0672	0.5176	0.4266	0.0155
1D-SL	0.8738	0.8203	0.0297	0.8767	0.7751	0.0485	0.8211	0.7401	0.0073
1D-SSL	0.9003	0.8496	0.0253	0.8868	0.7942	0.0416	0.8717	0.7650	0.0049
CL-SSL	0.9091	0.8624	0.0227	0.8973	0.8188	0.0380	0.8540	0.7516	0.0054
2D-SSL	0.9294	0.8652	0.0205	0.9103	0.8454	0.0316	0.9227	0.8516	0.0037
SC-JL	0.9178	0.8709	0.0218	0.9088	0.8346	0.0340	0.9167	0.8623	0.0038
BSFC-SSL	**0.9478**	**0.8981**	**0.0130**	**0.9181**	**0.8698**	**0.0202**	**0.9450**	**0.8838**	**0.0031**

performance improves progressively as the upper limit of the low-frequency band increases. The recovery of the long-wavelength background structure is notably more stable and accurate with the 5 Hz model, leading to the lowest final $\mathscr{L}_{\text{total}}$, whereas performance degrades gradually as the low-frequency content is reduced to 1 Hz. Optimal inversion results are achieved when the low-frequency model includes comprehensive parameters—P-wave velocity, S-wave velocity, and density. Notably, although the low-frequency model significantly influences the results, the variation in total loss $\mathscr{L}_{\text{total}}$ remains within a narrow range of 0.033–0.039. This range is substantially smaller than the effects induced by other factors, such as the number of convolutional layers in the BSFC network or the input width M. The BSFC-SSL framework is robust to imperfections in the low-frequency model; its semi-supervised and spatially constrained design ensures stable performance even when the low-frequency input is sparse or inaccurate.

4.6. Computational efficiency analysis

While the BSFC-SSL method demonstrates significant advantages in inversion accuracy and spatial continuity, its computational efficiency is also crucial for practical applications. To comprehensively evaluate the computational overhead of BSFC-SSL, we compared the training and inference times as well as the model parameter counts of 1D-SL, 1D-SSL, 2D-SSL, and BSFC-SSL methods under identical experimental conditions using the Marmousi2 model. As shown in Fig. 31, the computational time of BSFC-SSL was approximately 187 s, compared to 159 s for 2D-SSL, indicating an additional computational overhead of about 18% in BSFC-SSL. This increase is further reflected in the model parameter counts: BSFC-SSL comprises 104,905 parameters, compared to 94,758 for 2D-SSL, representing an 11% increase in model size. The increased computational cost and parameter count primarily stem from the introduction of the BSFC network. During training, the BSFC network requires additional operations for feature extraction and spatial constraint computation, including the recovery of parameters at non-well locations and the enforcement of self-consistency constraints. These operations increase the complexity of both forward and backward propagation in the network architecture. Although BSFC-SSL incurs higher computational time compared to 2D-SSL, it achieves substantial improvements in inversion accuracy (as evidenced by PCC, R^2, and RMSE metrics) and spatial continuity, particularly in complex geological regions and under conditions of sparse well constraints. Therefore, BSFC-SSL represents a favorable trade-off between accuracy and efficiency, making it particularly suitable for practical applications where inversion quality is paramount. In future work, we will focus on optimizing the BSFC network architecture through lightweight design or parallel computing strategies to reduce computational costs and enhance the real-time performance and scalability of the method. Such optimizations would be particularly beneficial for extending the BSFC-SSL framework to three-dimensional AVO inversion problems, where computational demands increase substantially with data volume and spatial complexity.

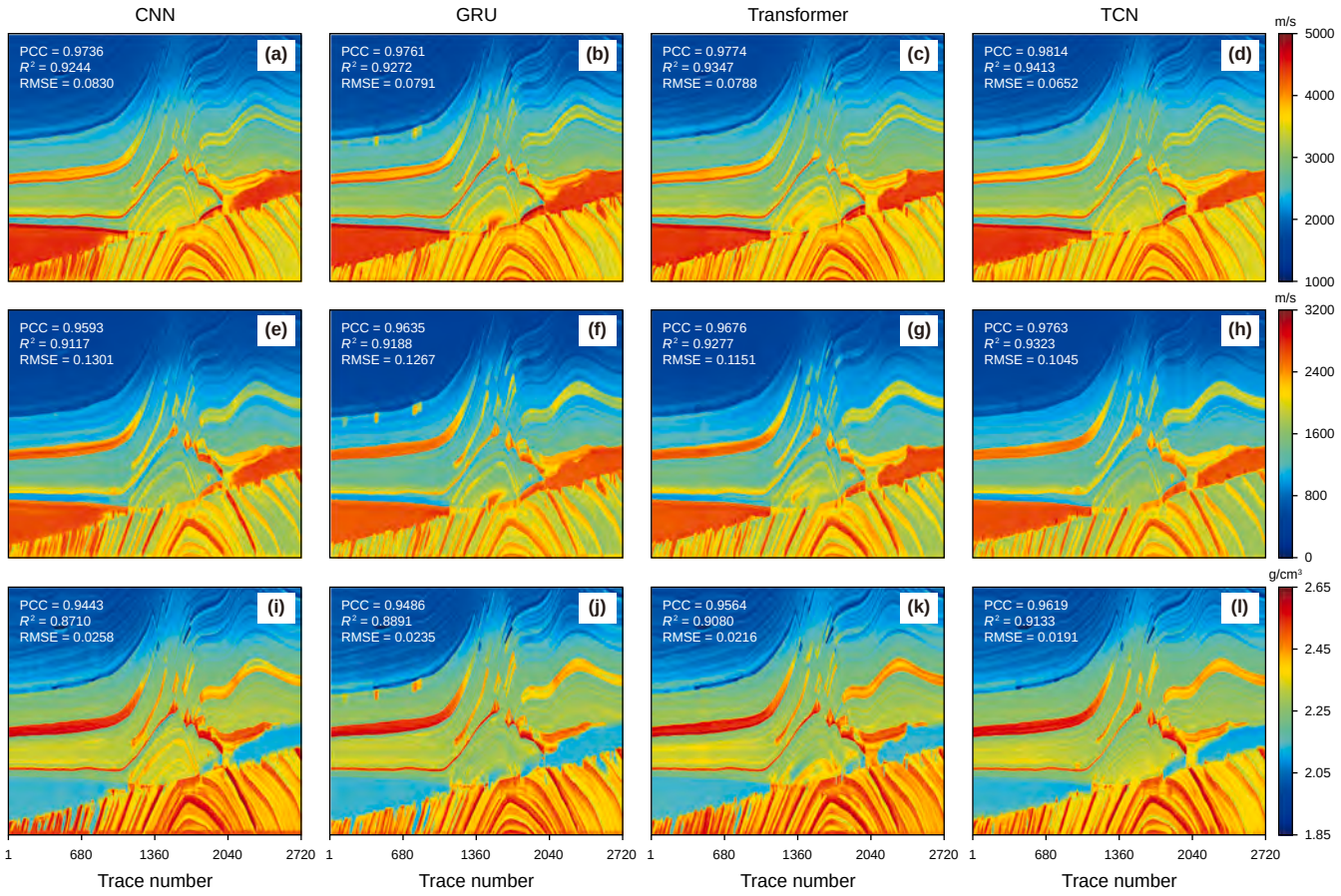

Fig. 26. Supervised inversion results for **(a)**–**(d)** P-wave velocity, **(e)**–**(h)** S-wave velocity, and **(i)**–**(l)** density obtained using different two-dimensional neural network architectures. The first column presents the CNN-based inversion results, the second column presents the GRU-based results, the third column presents the Transformer-based results, and the final column presents the TCN-based results. The evaluation score of each inversion result is displayed in the top-left corner of the corresponding subfigure.

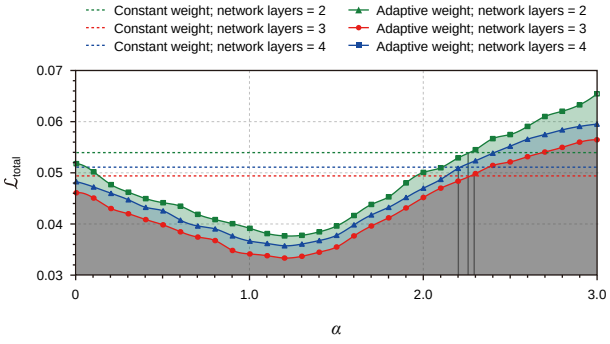

Fig. 27. The influence of different values of α and numbers of CNN layers within the BSFC network on $\mathscr{L}_{total}$.

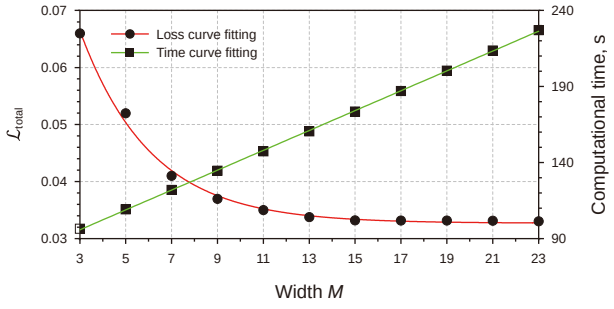

Fig. 28. Impact of width M on $\mathscr{L}_{total}$ and computational time.

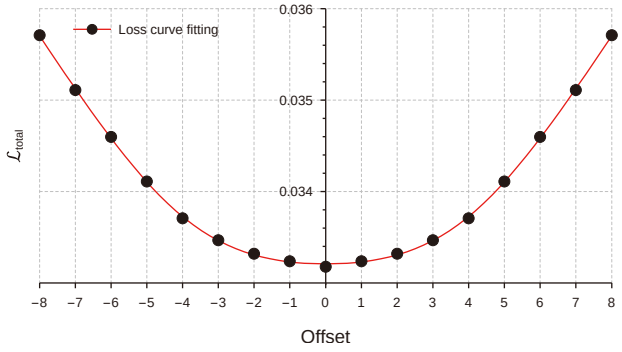

Fig. 29. The influence of the well-log location on $\mathcal{L}_{total}$. An offset of 0 indicates that the well-log is at the middle trace. Negative offset values correspond to shifts toward the left, while positive values indicate shifts toward the right.

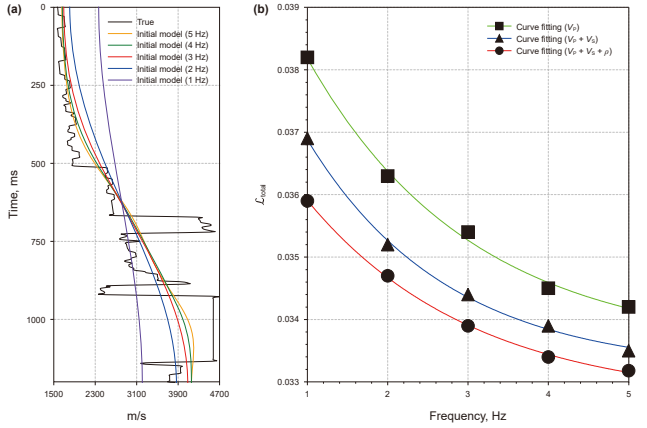

Fig. 30. Impact of the low-frequency model. **(a)** P-wave velocity from low-frequency models at trace 100 with different cutoff frequencies (1–5 Hz). **(b)** Variation of the total loss during training with different models.

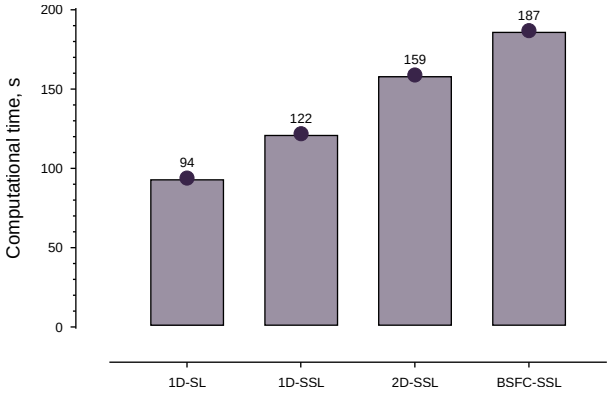

Fig. 31. Comparison of computational times among different methods.

5. Conclusion

In this article, we introduce the BSFC-SSL method, a novel approach to AVO inversion that addresses the limitations of traditional one-dimensional and two-dimensional DL methods. Unlike one-dimensional DL methods, which suffer from a lack of lateral continuity, and two-dimensional DL methods, which fail to fully utilize well-log data, the BSFC-SSL method addresses these challenges by integrating a label annihilation operator and a bidirectional spatial feature constraint (BSFC) network. This approach effectively constrains both well-log data and adjacent seismic traces, thereby improving both lateral continuity and inversion accuracy. Experimental results on both synthetic data and field data show that the BSFC-SSL method is superior to the model-based, one-dimensional DL, and two-dimensional DL methods in terms of lateral continuity and inversion accuracy.

CRediT authorship contribution statement

Ying-Tian Liu: Writing – review & editing, Writing – original draft, Visualization, Validation, Software, Resources, Methodology, Funding acquisition, Formal analysis, Conceptualization. **Yong Li:** Writing – review & editing, Writing – original draft, Visualization, Validation, Supervision, Project administration, Conceptualization. **Jun-Heng Peng:** Writing – review & editing, Writing – original draft, Visualization, Supervision, Methodology, Conceptualization. **Jian-Yong Xie:** Writing – review & editing, Supervision, Investigation, Funding acquisition, Conceptualization. **Xian-Qiong Chen:** Formal analysis, Resources, Visualization.

Declaration of competing interest

The authors declare that they have no known competing financial interests or personal relationships that could have appeared to influence the work reported in this paper.

Acknowledgments

This research is supported by the National Natural Science Foundation of China (42274175), Sichuan Provincial Joint Fund Project for Science, Technology and Education (2025LHJJ0347), Innovative Experimental Project at Institutions of Higher Education in Sichuan Province (Advanced Quantitative Rock Physics Investigations on the “Acoustic, Electrical, and Mechanical” Characteristics of Unconventional Reservoirs Subjected to Extreme High Temperature and High Pressure Environments) and the AI Research Fund of Chengdu University of Technology (grant No. 2025AI053).

References

Ahmed, N., Weibull, W.W., Grana, D., 2022. Constrained non-linear AVO inversion based on the adjoint-state optimization. Comput. Geosci. 168, 105214. https://doi.org/10.1016/j.cageo.2022.105214.

Ahmed, N., Weibull, W.W., Quintal, B., et al., 2023. Frequency-dependent AVO inversion applied to physically based models for seismic attenuation. Geophys. J. Int. 233 (1), 234–252. https://doi.org/10.1093/gji/ggac461.

Alemie, W., Sacchi, M.D., 2011. High-resolution three-term AVO inversion by means of a Trivariate Cauchy probability distribution. Geophysics 76 (3), R43–R55. https://doi.org/10.1190/1.3554627.

Alfarraj, M., AlRegib, G., 2019. Semisupervised sequence modeling for elastic impedance inversion. Interpretation 7 (3), SE237–SE249. https://doi.org/10.1190/INT-2018-0250.1.

Avseth, P., Janke, A., Horn, F., 2016. AVO inversion in exploration—Key learnings from a Norwegian Sea prospect. Lead. Edge 35 (5), 405–414. https://doi.org/10.1190/tle35050405.1.

Bortfeld, R., 1961. Approximations to the reflection and transmission coefficients of plane longitudinal and transverse waves. Geophys. Prospect. 9 (4), 485–502. https://doi.org/10.1111/j.1365-2478.1961.tb01670.x.

Cao, D., An, P., Liu, S., 2018. Elastic-Parameters Inversion from EI Based on the deep-learning Method, 2018. SEG Technical Program Expanded Abstracts, pp. 640–644. https://doi.org/10.1190/segam2018-2998479.1.

Chen, W., Yang, L., Zha, B., et al., 2020. Deep learning reservoir porosity prediction based on multilayer long short-term memory network. Geophysics 85 (4), WA213–WA225. https://doi.org/10.1190/geo2019-0261.1.
Chen, Z., Badrinarayanan, V., Lee, C.Y., et al., 2018. Gradnorm: Gradient normalization for adaptive loss balancing in deep multitask networks. In: Proceedings of the 35th International Conference on Machine Learning, PMLR 80, pp. 794–803.
Das, V., Pollack, A., Wollner, U., et al., 2019. Convolutional neural network for seismic impedance inversion. Geophysics 84 (6), R869–R880. https://doi.org/10.1190/geo2018-0838.1.
Di, H., Li, Z., Maniar, H., et al., 2020. Seismic stratigraphy interpretation by deep convolutional neural networks: a semisupervised workflow. Geophysics 85 (4), WA77–WA86. https://doi.org/10.1190/geo2019-0433.1.
Dong, S., Yang, X., Xu, T., et al., 2024. Semi-supervised neural network for complex lithofacies identification using well logs. IEEE Trans. Geosci. Rem. Sens. 62, 1–19. https://doi.org/10.1109/TGRS.2024.3450103.
Dong, S., Zeng, L., Lyu, W., et al., 2020. Fracture identification by semi-supervised learning using conventional logs in tight sandstones of Ordos Basin, China. J. Nat. Gas Sci. Eng. 76, 103131. https://doi.org/10.1016/j.jngse.2019.103131.
Dou, Y., Li, K., Zhu, J., et al., 2022. Efficient training of 3-D seismic fault segmentation network under sparse labels by weakening anomaly annotation. IEEE Trans. Geosci. Rem. Sens. 60, 1–14. https://doi.org/10.1109/TGRS.2022.3196810.
Dou, Y., Li, K., Zhu, J., et al., 2021. Attention-based 3-D seismic fault segmentation training by a few 2-D slice labels. IEEE Trans. Geosci. Rem. Sens. 60, 1–15. https://doi.org/10.1109/TGRS.2021.3113676.
Downton, J.E., Hampson, D.P., GeoSoftware, C., 2019. Use of theory-guided Neural Networks to Perform Seismic Inversion. In: GeoConvention 2019.
Downton, J.E., Ursenbach, C., 2006. Linearized amplitude variation with offset (AVO) inversion with supercritical angles. Geophysics 71 (5), E49–E55. https://doi.org/10.1190/1.2227617.
Fabien-Ouellet, G., Sarkar, R., 2020. Seismic velocity estimation: A deep recurrent neural-network approach. Geophysics 85 (1), U21–U29. https://doi.org/10.1190/geo2018-0786.1.
Feng, W., Liu, Y., Li, Y., et al., 2025. Acoustic impedance prediction using an attention-based dual-branch double-inversion network. Earth Sci. Inf. 18, 1–20. https://doi.org/10.1007/s12145-024-01548-4.
Fu, Z., Yin, C., Chen, T., et al., 2024. Using the wavelet transform for seismic wave impedance inversion. Geophysics 89 (5), R387–R397. https://doi.org/10.1190/geo2023-0415.1.
Ge, Q., Cao, H., Yang, Z., et al., 2024. Deep learning-based pre-stack seismic inversion constrained by AVO attributes. IEEE Geosci. Rem. Sens. Letters 21, 1–5. https://doi.org/10.1109/LGRS.2024.3373197.
Gray, D., Andersen, E., 2000. The application of AVO and inversion to the estimation of rock properties. SEG Tech. Progr. Expand. Abstr. 549–552. https://doi.org/10.1190/1.1816120, 2000.
Gu, X., Lu, W., Li, Y., et al., 2023. Semi-supervised seismic stratigraphic interpretation constrained by spatial structure. IEEE Trans. Geosci. Rem. Sens. 61, 1–10. https://doi.org/10.1109/TGRS.2023.3288668.
Guo, R., Zhang, J., Liu, D., et al., 2019. Application of bi-directional long short-term memory recurrent neural network for seismic impedance inversion. In: 81st EAGE Conference and Exhibition. https://doi.org/10.3997/2214-4609.201901386.
Ikelle, L., 1995. Linearized inversion of 3-D multi-offset data: background reconstruction and AVO inversion. Geophys. J. Int. 123 (2), 507–528. https://doi.org/10.1111/j.1365-246X.1995.tb06868.x.
Jensen, E.H., Johansen, T.A., Avseth, P., et al., 2016. Quantitative interpretation using inverse rock-physics modeling on AVO data. Lead. Edge 35 (8), 677–683. https://doi.org/10.1190/tle35080677.1.
Li, K., Dou, Y., Xiao, Y., et al., 2024. TransInver: 3D data-driven seismic inversion based on self-attention. Geophysics 89 (1), WA127–WA141. https://doi.org/10.1190/geo2023-0144.1.
Li, K., Li, K., Yin, X., et al., 2022a. Hierarchical Bayesian probabilistic seismic AVO inversion using Gibbs sampling with IA2RMS algorithm. IEEE Geosci. Rem. Sens. Letters 19, 1–5. https://doi.org/10.1109/LGRS.2022.3181816.
Li, Z., Chen, X., Li, J., et al., 2022b. Pertinent multigate mixture-of-experts-based prestack three-parameter seismic inversion. IEEE Trans. Geosci. Rem. Sens. 60, 1–15. https://doi.org/10.1109/TGRS.2022.3208226.
Liao, Z., Li, Y., Xia, E., et al., 2023. A twice denoising autoencoder framework for random seismic noise attenuation. IEEE Trans. Geosci. Rem. Sens. 61, 1–15. https://doi.org/10.1109/TGRS.2023.3244034.
Liu, B., Jiang, P., Wang, Q., et al., 2023. Physics-driven self-supervised learning system for seismic velocity inversion. Geophysics 88 (2), R145–R161. https://doi.org/10.1190/geo2021-0302.1.
Liu, X., Wu, B., Wei, C., et al., 2024. InverMulT-STP: Closed-loop transformer seismic AVA inversion with synthetic data style transfer pretraining. IEEE Trans. Geosci. Rem. Sens. 62, 4507418. https://doi.org/10.1109/TGRS.2024.3409450.
Liu, Y., Li, Y., Li, H., et al., 2025a. Nash-multitask learning-semisupervised temporal convolutional network method for prestack three-parameter inversion. Geophysics 90 (4), R175–R193. https://doi.org/10.1190/geo2024-0417.1.
Liu, Y., Li, Y., Peng, J., et al., 2025b. High-resolution closed-loop seismic inversion network in the time-frequency-phase mixed domain. Geophysics 90 (6), M271–M288. https://doi.org/10.1190/geo2024-0573.1.
Masroor, M., Niri, M.E., Sharifinasab, M.H., 2023. A multiple-input deep residual convolutional neural network for reservoir permeability prediction. Geoenergy Sci. Eng. 222, 211420. https://doi.org/10.1016/j.geoen.2023.211420.
Meng, J., Wang, S., Cheng, W., et al., 2021. AVO inversion based on transfer learning and low-frequency model. IEEE Geosci. Rem. Sens. Letters 19, 3004605. https://doi.org/10.1109/LGRS.2021.3132426.
Misra, S., Sacchi, M.D., 2008. Global optimization with model-space preconditioning: Application to AVO inversion. Geophysics 73 (5), R71–R82. https://doi.org/10.1190/1.2958008.
Mustafa, A., Alfarraj, M., AlRegib, G., 2019. Estimation of acoustic impedance from seismic data using temporal convolutional network. SEG Tech. Progr. Expand. Abstr. 2554–2558. https://doi.org/10.1190/segam2019-3216840.1, 2019.
Mustafa, A., Alfarraj, M., AlRegib, G., 2021. Joint learning for spatial context-based seismic inversion of multiple data sets for improved generalizability and robustness. Geophysics 86 (4), O37–O48. https://doi.org/10.1190/geo2020-0432.1.
Navon, A., Shamsian, A., Achituve, I., et al., 2022. Multi-task learning as a bargaining game. arXiv preprint. https://doi.org/10.48550/arXiv.2202.01017.
Peng, J., Liu, Y., Wang, M., et al., 2024. Zero-shot self-consistency learning for seismic irregular spatial sampling reconstruction. arXiv preprint. https://doi.org/10.48550/arXiv.2411.00911.
Pourpanah, F., Abdar, M., Luo, Y., et al., 2022. A review of generalized zero-shot learning methods. IEEE Trans. Pattern Anal. Mach. Intell. 45 (4), 4051–4070. https://doi.org/10.1109/TPAMI.2022.3191696.
Sang, W., Yuan, S., Han, H., et al., 2023. Porosity prediction using semi-supervised learning with biased well log data for improving estimation accuracy and reducing prediction uncertainty. Geophys. J. Int. 232 (2), 940–957. https://doi.org/10.1093/gji/ggac371.
She, B., Wang, Y., Zhang, J., et al., 2019. AVO inversion with high-order total variation regularization. J. Appl. Geophys. 161, 167–181. https://doi.org/10.1016/j.jappgeo.2018.12.014.
Shi, S., Li, M., Wang, J., et al., 2024. Seismic impedance inversion based on semi-supervised learning. Comput. Geosci. 182, 105497. https://doi.org/10.1016/j.cageo.2023.105497.
Smith, G., Gidlow, P., 1987. Weighted stacking for rock property estimation and detection of gas. Geophys. Prospect. 35 (9), 993–1014. https://doi.org/10.1111/j.1365-2478.1987.tb00856.x.
Sun, J., Innanen, K.A., Huang, C., 2021. Physics-guided deep learning for seismic inversion with hybrid training and uncertainty analysis. Geophysics 86 (3), R303–R317. https://doi.org/10.1190/geo2020-0312.1.
Wang, B., Han, D., Li, J., 2022a. Missing shots and near-offset reconstruction of marine seismic data with towered streamers via self-supervised deep learning. IEEE Trans. Geosci. Rem. Sens. 60, 1–9. https://doi.org/10.1109/TGRS.2022.3172145.
Wang, H., Yan, J., Fu, G., et al., 2020a. Current status and application prospect of deep learning in geophysics. Prog. Geophys. 35 (2), 642–655. https://doi.org/10.6038/pg2020CC0476 (in Chinese).
Wang, Q., Wang, Y., Ao, Y., et al., 2022b. Seismic inversion based on 2D-CNNs and domain adaption. IEEE Trans. Geosci. Rem. Sens. 60, 5921512. https://doi.org/10.1109/TGRS.2022.3213337.
Wang, S., Si, X., Cai, Z., et al., 2024. Fast global self-attention for seismic image fault identification. IEEE Trans. Geosci. Rem. Sens. 62, 1–11. https://doi.org/10.1109/TGRS.2024.3436066.
Wang, X., Wei, J., Schuurmans, D., et al., 2022c. Self-consistency improves chain of thought reasoning in language models. arXiv preprint. https://doi.org/10.48550/arXiv.2203.11171.
Wang, Y., Wang, B., Tu, N., et al., 2020b. Seismic trace interpolation for irregularly spatial sampled data using convolutional autoencoder. Geophysics 85 (2), V119–V130. https://doi.org/10.1190/geo2018-0699.1.
Wang, Z., Wang, S., Zhou, C., et al., 2023. AVO inversion based on closed-loop multitask conditional Wasserstein generative adversarial network. IEEE Trans. Geosci. Rem. Sens. 61, 1–13. https://doi.org/10.1109/TGRS.2023.3260908.
Wu, X., Yan, S., Bi, Z., et al., 2021. Deep learning for multidimensional seismic impedance inversion. Geophysics 86 (5), R735–R745. https://doi.org/10.1190/geo2020-0564.1.
Xiong, W., Ji, X., Ma, Y., et al., 2018. Seismic fault detection with convolutional neural network. Geophysics 83 (5), O97–O103. https://doi.org/10.1190/geo2017-0666.1.
Yang, F., Ma, J., 2019. Deep-learning inversion: A next-generation seismic velocity model building method. Geophysics 84 (4), R583–R599. https://doi.org/10.1190/geo2018-0249.1.
Yin, X.Y., Deng, W., Zong, Z.Y., 2016. AVO inversion based on inverse operator estimation in trust region. J. Geophys. Eng. 13 (2), 194–206. https://doi.org/10.1088/1742-2132/13/2/194.
Yuan, S., Jiao, X., Luo, Y., et al., 2022. Double-scale supervised inversion with a data-driven forward model for low-frequency impedance recovery. Geophysics 87, R165–R181. https://doi.org/10.1190/geo2020-0421.1.

Zhang, J., Li, J., Chen, X., et al., 2021. Robust deep learning seismic inversion with a priori initial model constraint. Geophys. J. Int. 225 (3), 2001–2019. https://doi.org/10.1093/gji/ggab074.
Zhang, J., Sun, H., Zhang, G., et al., 2022. Deep learning seismic inversion based on prestack waveform datasets. IEEE Trans. Geosci. Rem. Sens. 60, 1–11. https://doi.org/10.1109/TGRS.2022.3195858.
Zhao, Y., Li, Y., Dong, X., et al., 2018. Low-frequency noise suppression method based on improved DnCNN in desert seismic data. IEEE Geosci. Rem. Sens. Letters 16 (5), 811–815, 0.1109/LGRS.2018.2882058.
Zheng, Y., Zhang, Q., Yusifov, A., et al., 2019. Applications of supervised deep learning for seismic interpretation and inversion. Lead. Edge 38 (7), 526–533. https://doi.org/10.1190/tle38070526.1.
Zoeppritz, K., 1919. On the reflection and propagation of seismic waves. Gottinger Nachrichten 1, 66–84.
Zong, Z.Y., Yin, X.Y., Li, K., 2016. Joint AVO inversion in the time and frequency domain with Bayesian interference. Appl. Geophys. 13, 631–640. https://doi.org/10.1007/s11770-016-0584-7.